

The Massive and Distant Clusters of WISE Survey 2: Splashback Radii to $z=1.65$ from Galaxy Density Profiles

KHUNANON THONGKHAM ,^{1,2,3} ANTHONY H. GONZALEZ ,³ MARK BRODWIN ,⁴ ARIANE TRUDEAU ,^{3,5}
 PETER EISENHARDT,⁶ S. A. STANFORD ,⁷ EMILY MORAVEC ,⁸ THOMAS CONNOR ,⁹ AND DANIEL STERN ⁶

¹ National Astronomical Research Institute of Thailand (NARIT), Mae Rim, Chiang Mai 50180, Thailand

² Korea Astronomy and Space Science Institute, 776, Daedeokdae-ro, Yuseong-gu, Daejeon 34055, Republic of Korea

³ Department of Astronomy, University of Florida, 211 Bryant Space Center, Gainesville, FL 32611, USA

⁴ Eureka Scientific, 2452 Delmer Street Suite 100, Oakland, CA, 94602-3017, USA

⁵ Institute of Astronomy and Astrophysics, Academia Sinica, Taipei 10617, Taiwan

⁶ Jet Propulsion Laboratory, California Institute of Technology, 4800 Oak Grove Dr., Pasadena, CA 91109, USA

⁷ Department of Physics, University of California, One Shields Avenue, Davis, CA 95616, USA

⁸ Green Bank Observatory, P.O. Box 2, Green Bank, WV 24944

⁹ Center for Astrophysics | Harvard & Smithsonian, 60 Garden St., Cambridge, MA 02138, USA

(Received XXX; Revised XXX; Accepted XXX)

Submitted to ApJ

ABSTRACT

The Massive and Distant Clusters of WISE Survey 2 (MaDCoWS2) is a WISE-selected catalog of galaxy clusters at $0.1 < z < 2$ covering an effective area of $> 6000 \text{ deg}^2$. In this paper, we derive splashback radii for this cluster ensemble from galaxy density profiles and constrain the mass threshold of the survey as a function of redshift. We use MaDCoWS2 cluster candidates at $0.4 \leq z \leq 1.65$ divided into subsamples with different signal-to-noise (S/N_P) and redshifts, cross-correlated with galaxies from the CatWISE2020 catalog, to obtain average surface density profiles. We perform a Markov Chain Monte Carlo analysis to derive parameter estimates for theoretical models consisting of orbiting and infalling terms. A distinct splashback feature is detected in all subsamples. The measured splashback radii span from $0.89^{+0.02}_{-0.02} h^{-1}$ comoving Mpc/cMpc ($0.61^{+0.02}_{-0.02} h^{-1}$ proper Mpc/pMpc) at $\bar{z} = 0.45$ to $1.27^{+0.05}_{-0.05} h^{-1}$ cMpc ($0.53^{+0.04}_{-0.04} h^{-1}$ pMpc) at $\bar{z} = 1.54$. We also find that splashback radii increase with S/N_P at fixed redshift. The resultant splashback radii constrain the redshift dependence of the mass of MaDCoWS2 clusters at fixed S/N_P . We calculate M_{200m} from the radii using a relation based on a cosmological simulation. MaDCoWS2 M_{200m} values derived from the simulation-based relation are lower than the expected values based on weak-lensing observations. More robust mass constraints will come from calibrating splashback radii derived from galaxy density profiles with weak lensing shear profiles from facilities such as *Euclid*, *Rubin*, and *Roman*.

Keywords: — Catalogs (205) — Surveys (1671) — Galaxy clusters (584) — High-redshift galaxy clusters (2007) — Large-scale structure of the universe (902)

1. INTRODUCTION

In recent decades, galaxy clusters have played a crucial role in advancing our understanding of cosmology (e.g. A. Vikhlinin et al. 2009; S. W. Allen et al. 2011) and astrophysics (A. von der Linden et al. 2010; A. C. Fabian 2012; B. R. McNamara & P. E. J. Nulsen 2012; S. Alberts & A. Noble 2022; C. M. Harrison & C. Ramos Almeida 2024). Because gravitational collapse occurs more rapidly in a high-density universe, the number of

galaxy clusters as a function of mass is a strong function of the matter density of the Universe. The amplitude of the mass function is also sensitive to the amplitude of the power spectrum on the scale of $8h^{-1}$ Mpc or σ_8 , which is related to matter density fluctuations (S. Bocquet et al. 2019; S. Grandis et al. 2024). The evolution of the mass function depends on the age of the Universe at a given redshift, and thus the mass function also probes dark energy (C. Heneka et al. 2018; F. Pacaud et al.

2018). Constraints derived from the mass function rely on having accurate, low-scatter cluster mass proxies because of the power law dependence of the mass function on cluster mass (J. Tinker et al. 2008; W. A. Watson et al. 2013; G. Despali et al. 2016; R. Seppi et al. 2021). A common approach to evaluating mass proxies is to define cluster masses and radii in terms of overdensity thresholds relative to the mean or critical density of the Universe. However, these mass definitions are not directly observable quantities. Furthermore, being tied to cosmology, they undergo pseudo-evolution as the matter density of the Universe changes with redshift.

The splashback radius has been suggested by B. Diemer & A. V. Kravtsov (2014); S. Adhikari et al. (2014); S. More et al. (2015) as an alternative to radii based on overdensity to minimize the impact of such issues. The splashback radius is defined as the radius where particles reach the apocenter of their first orbit, observationally characterized by the logarithmic slope of the density distribution showing a deep drop (S. More et al. 2015). In the case of spherical symmetry, this radius indicates a distinct boundary between infalling matter and matter that is already orbiting within the halo. Given a measured splashback radius, one can then measure observables within this radius that are expected to correlate with mass, such as weak lensing shear, without the added degeneracy associated with overdensity masses (C. Giocoli et al. 2024). Additionally, the splashback radius alone can be used as a mass proxy if one assumes a functional form for the cluster mass profile (O. Contigiani et al. 2023). The splashback radius could also provide a competitive constraint on cosmological parameters by comparing with results from simulation because it breaks the degeneracy between Ω_M and σ_8 (R. Haggar et al. 2024; C. T. Mpetha et al. 2024, 2025).

Many studies using cosmological simulations have investigated the physical interpretation of the splashback radius. S. O’Neil et al. (2021) confirmed the detection of the splashback feature in dark matter, gas, and satellite galaxies in hydrodynamical simulations such as IllustrisTNG. Using the Hydrangea simulations, O. Contigiani et al. (2021) found correlations between the splashback radius, the direction of the filaments, and the orientation of brightest cluster galaxies. T.-h. Shin & B. Diemer (2023) demonstrated that the splashback radius is a clean tracer of halo growth over its past dynamical time. More recently, K. Walker et al. (2025) showed that the splashback feature traced by stellar mass closely coincides with that of the dark matter distribution in GIZMO simulations from the Three Hundred Project. In addition, several models have been proposed to predict the splashback radius B. Diemer & A. V. Kravtsov

(2014); S. Adhikari et al. (2014); S. More et al. (2015); X. Shi (2016); P. Mansfield et al. (2017); B. Diemer et al. (2017); B. Diemer (2023). Across these studies, the mass accretion rate of dark matter halos consistently exhibits a tight correlation with the splashback radius. This establishes the splashback radius as a powerful probe of cluster assembly history.

The first significant observational detection of splashback radius comes from S. More et al. (2016) using cross-correlation between the redMaPPer Sloan Digital Sky Survey (SDSS) clusters (E. S. Rykoff et al. 2014) and SDSS galaxies. Following this work, detections of splashback radii have been made by multiple investigators using different galaxy cluster surveys. On the optical/infrared side, detections of splashback radii were shown in redMaPPer Dark Energy Survey (DES) clusters (E. Baxter et al. 2017; C. Chang et al. 2018), Hyper Suprime-Cam (HSC) CAMIRA clusters (A. J. Nishizawa et al. 2018; R. Murata et al. 2020), Adaptive Matched Identifier of Clustered Objects in Kilo-Degree Survey Data Release 3 (AMICO KiDS-DR3) clusters (C. Giocoli et al. 2024), and Dark Energy Spectroscopic Instrument (DESI) Legacy Imaging Surveys (LS) clusters (W. Xu et al. 2024) using cluster weak lensing and/or cluster-galaxy cross-correlation. For surveys based on Sunyaev–Zeldovich (SZ) detections, the splashback radius has been detected in the Planck cluster catalog (D. Zurcher & S. More 2019) and a catalog combining the Atacama Cosmology Telescope (ACT) and the South Pole Telescope (SPT) cluster catalogs (T. Shin et al. 2019, 2021), all using cluster-galaxy cross-correlation and weak lensing. For X-ray based surveys, the splashback radius has been observed in the weak lensing of the Cluster Lensing And Supernova survey with Hubble (CLASH) clusters (K. Umetsu & B. Diemer 2017) and the Canadian Cluster Comparison Project (CCCP) clusters (O. Contigiani et al. 2019). M. Bianconi et al. (2021) presents the splashback feature in a stacked luminosity density profile. The eROSITA Final Equatorial-Depth Survey (eFEDS) also shows the splashback radius based on cross-correlation measurement in D. Rana et al. (2023).

All of these previous works utilize cluster catalogs that are limited to $z < 1$. The redshift, mass range ($0.1 < z < 2$, $M > 1 \times 10^{13} M_\odot$, K. Thongkham et al. 2024a,b), and large sample size of MaDCoWS2 provide the first opportunity to measure the splashback feature for a uniform cluster sample out to an epoch where changes in cluster scales are expected to be significant.

In this work, we use cross-correlation between MaDCoWS2 cluster candidates and WISE galaxies to investigate the MaDCoWS2 cluster profiles and detect the

splashback radius at $0.4 < z < 1.65$. We also explore the dependence of the splashback radius on redshift and S/N_p (Signal-to-noise under the assumption that the noise can be approximated as Poissonian) for the MaDCoWS2 sample. This is the first step towards an independent assessment of the radial boundary and characteristic mass limit of the MaDCoWS2 clusters as a function of their redshift and S/N_p .

Section 2 describes the cluster and galaxy catalogs used in this paper. Section 3 details the methodology, explaining the surface density measurement, the model used, and the model fitting method. We present the density profiles based on the cross-correlation and the splashback radius measurements in Section 4, while also discussing the implications of these results. We summarize our conclusions in Section 5.

Throughout this paper, we assume a flat Λ CDM cosmology from [Planck Collaboration et al. \(2020\)](#) with $\Omega_m = 0.315$ and $H_0 = 67.4 \text{ km s}^{-1} \text{ Mpc}^{-1}$. In Tables and Figures however, we report quantities with a dimensionless Hubble parameter h where $H_0 = 100 \text{ } h \text{ km s}^{-1} \text{ Mpc}^{-1}$ to facilitate comparison with other studies. Distances in the comoving and proper frames are denoted by cMpc and pMpc respectively. R and r denote the projected and three-dimensional radii, respectively.

2. DATA

2.1. *MaDCoWS2 clusters*

The MaDCoWS2 catalog ([K. Thongkham et al. 2024a,b](#)) consists of 133,036 cluster candidates with $S/N_p \geq 5$ at $0.1 < z < 2$. The galaxy clusters in the catalog are detected using CatWISE2020-selected galaxies ([P. R. M. Eisenhardt et al. 2020](#); [F. Marocco et al. 2021](#)). Photometric redshift probability distribution functions (PDFs) are derived for each galaxy using g , r , z , W_1 , and W_2 data from the ninth data release of Dark Energy Camera Legacy Survey (DECaLS DR9, see [A. Dey et al. 2019](#)) and from CatWISE2020 (see §2.2). The search identifies the overdensities of galaxies in three dimensions (sky positions and photometric redshifts) using the PZWav algorithm ([A. Gonzalez 2014](#); [Euclid Collaboration et al. 2019](#); [S. V. Werner et al. 2023](#); [K. Thongkham et al. 2024a,b](#); [Euclid Collaboration et al. 2025](#)). This catalog covers 6498 (8436 without masking) deg^2 spanning the majority of the DECaLS area.

Our analysis considers cluster candidates divided into subsamples according to their properties, specifically photometric redshift and S/N_p , where S/N_p is defined as the signal-to-noise ratio of high-density peaks in a three-dimensional galaxy density cube relative to the noise estimated from a random density cube assum-

ing that it follows a Poisson distribution. We divide the cluster sample into multiple subsamples with photometric redshift and S/N_p bins shown in Figure 1, within which we calculate the mean cluster-galaxy cross-correlations to estimate the projected galaxy density around each cluster subsample. The number of cluster candidates in each subsample selection is provided in Table 1. This subdivision is designed to facilitate comparison with [A. Trudeau et al. \(2024\)](#).

We focus on cluster candidates at $0.4 < z < 1.65$ in this work. This redshift range ensures a low level of systematic and statistical uncertainties in the density profile measurements. Outside this redshift range, the identification of a splashback radius with well-constrained uncertainty from the galaxy density profile becomes harder. Our cut based on absolute W1 magnitude results in a smaller number of galaxies at $z < 0.4$. At $z > 1.65$, the number of clusters is low due to the photometric limits of the galaxy and cluster catalogs. This leads to a higher variance in the galaxy density outside of the core profile and prevents a robust measurement of the splashback radius in these redshift ranges.

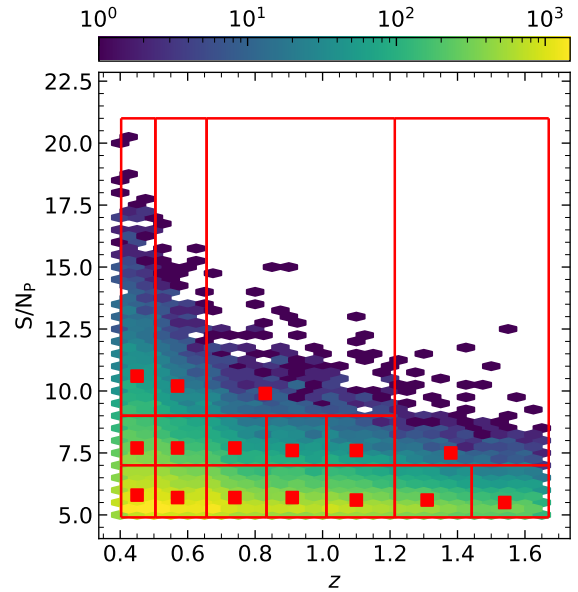


Figure 1. Sample selection of the cluster candidates used in the analysis of this paper. The cluster sample is displayed in hexagonal bins with a bin size of 0.05 in cluster redshift on the x-axis and 0.5 in S/N_p on the y-axis. S/N_p and z are the signal-to-noise ratio and photometric redshift of the clusters. Bin colors indicate the number of clusters. The solid red lines display the binning scheme for subsamples shown in Table 1. The red squares indicate \bar{S}/N_p and \bar{z} of the subsamples.

Table 1. Cluster counts in each bin, organized by redshift (first column) and S/N_P (three other columns.)

z	$5 \leq S/N_P < 7$	$7 \leq S/N_P < 9$	$S/N_P \geq 9$
0.4-0.5	15613	4724	2065
0.5-0.65	19382	4139	1088
0.65-0.83	15667	2255	...
0.83-1.0	11439	1381	...
1.0-1.2	10862	917	...
1.2-1.43	8108
1.43-1.65	4843
1.2-1.65	...	637	...
0.65-1.2	612

2.2. Galaxy catalogs

We use the galaxy catalogs built for the MaDCoWS2 cluster search as the primary input of the galaxy cross-correlation analysis. We refer readers to [K. Thongkham et al. \(2024a\)](#) for a detailed description of the process, which we summarize below.

The positions of the galaxies in this analysis are from the infrared CatWISE2020 catalog. We employ the same filtering and masking procedures as in MaDCoWS2 on the galaxy sample. This includes filtering artifacts based on artifact flags from CatWISE2020 and DECaLS, removing stars based on $r - z$ and $z - W1$ colors, and removing galaxies using large galaxy masks and bright star masks. We also reject galaxies with a low probability of being a match between CatWISE2020 and DECaLS. The galaxy catalog used in MaDCoWS2 also requires DECaLS detections, which hinders the detection S/N for the highest-z clusters. To prevent faint galaxies from significantly contributing to the correlation estimate of the subsample at low redshift, we employ an absolute magnitude cut of $M = -23.01$ AB in the WISE W1 band, equivalent to an apparent magnitude of $W1 = 18.74$ AB at $z = 0.4$ and $W1 = 23$ AB at $z = 2$.

The galaxy selection can impact the redshift dependence of the derived radii if the splashback radius is dependent upon either galaxy mass or galaxy color. Selections based on artifact flags, stellar rejection, and masking should not introduce redshift or mass-dependent biases to our analysis. Selecting galaxies down to a constant absolute magnitude should minimize any dependence on galaxy mass since it ensures similar galaxies are being looked at in each redshift bin. Requiring 5-band photometry will have some impact at high redshift. Due the magnitude limit of our galaxy catalog, we would

start losing a lot of galaxies only at the highest redshift bins. Nevertheless, it has also been argued in [R. Murata et al. \(2020\)](#) that the splashback radius constraint is not strongly dependent on color up to $z < 1$, so we do not expect the bias from our selection to be strong.

3. GALAXY NUMBER DENSITY

3.1. Measurement

We measure the galaxy surface density around our clusters using cluster galaxy cross-correlation similar to the correlation performed in [T. Shin et al. \(2019, 2021\)](#) and [R. Murata et al. \(2020\)](#). We use a modified version of the Landy-Szalay estimator ([S. D. Landy & A. S. Szalay 1993](#)) to calculate the two-point cross correlation between MaDCoWS2 clusters and the galaxy sample in §2.2. The estimator follows the equation

$$\omega(\theta) = \frac{D_c D_g - D_c R_g - R_c D_g + R_c R_g}{R_c R_g}, \quad (1)$$

where we compute normalized pairs of objects as a function of angular separation. The normalization is calculated with respect to the total number of pairs processed. D and R denote objects in the true and random catalogs, respectively, while the subscripts c and g refer to clusters and galaxies, respectively. We use a random cluster catalog with 100 times the number of galaxy clusters in our sample. The random galaxy data has 4 times the surface number density of the galaxy catalog. Survey masks are included when generating the random catalogs.

Each cluster subsample is divided into another set of subsamples with redshift binning of $\Delta z = 0.025$. For each of these subsample bins, we use `treecorr` ([M. Jarvis et al. 2004; M. Jarvis 2015](#)) to estimate angular two-point cross-correlations that we convert into comoving radial correlations using the angular diameter distance at the midpoint of the redshift bin. The correlation is computed over 40 comoving radial bins evenly divided in logarithmic space from 0.2 to $5 h^{-1}$ Mpc for all subsamples except for those with $S/N_P \geq 9$. By visual inspection and initial model fitting, we find that the infalling profile of those subsamples is not fully captured by the default radius limits of $5 h^{-1}$ Mpc. Thus, we use 50 bins from 0.2 to $8 h^{-1}$ Mpc instead for the $S/N_P \geq 9$ subsamples to ensure their entire halo profiles are captured by our analysis.

Across all subsamples, the maximum radial bin sizes are smaller than the median projected separation between clusters, S_{proj} . S_{proj} varies from 5.2 Mpc at $5 \leq S/N_P < 7$ and $0.4 < z < 0.5$ to 39.5 Mpc at $S/N_P \geq 9$ and $0.65 < z < 1.2$. The fraction of clusters overlapping in projection, defined as the fraction of overlap within $2 h^{-1}$ Mpc, correspondingly decreases from 11% to 1%

across these bins. Consequently, we do not expect projected cluster overlap to significantly affect our splashback radius measurements.

From the projected comoving radius R , we calculate the mean 2-point cross-correlation $\omega(R)$ for a larger redshift bin with $\Delta z = 0.3$ by averaging the correlations using weights from the number of clusters in each redshift bin following

$$\omega(R) = \frac{\sum_i N_{cl,i} \omega(R, z_i)}{\sum_i N_{cl,i}}, \quad (2)$$

where $N_{cl,i}$ is the number of cluster in each $\Delta z = 0.025$ redshift bin and $\omega(R, z_i)$ is the correlation of that small redshift bin. The mean subtracted projected galaxy profile $\Sigma_g(R)$ then can be obtained by

$$\Sigma_g(R) = \bar{\Sigma}_g \omega(R), \quad (3)$$

where $\bar{\Sigma}_g$ is the average surface number density of the sample of galaxy described by

$$\bar{\Sigma}_g = \frac{\sum_i N_{cl,i} \bar{\Sigma}_{g,i}}{\sum_i N_{cl,i}} \quad (4)$$

where $\bar{\Sigma}_{g,i}$ is the galaxy average surface number density in each small redshift bin calculated by dividing the number of galaxies within the bin by the surface area in h^{-2} cMpc 2 . We estimate the covariance matrix of the cross-correlation using a jackknife resampling method (P. Norberg et al. 2009), available as a part of `treecorr`, with 200 patches of approximately equal size with each patch representing a subdivision of the survey area. The jackknife resampling estimates the covariance matrix from correlations measured when one patch at a time is excluded from the sample with this process repeating until the total number of patches has been reached. The matrix can be described by

$$C = \frac{N_{\text{patch}} - 1}{N_{\text{patch}}} \sum_i (\omega_i - \bar{\omega})^T (\omega_i - \bar{\omega}). \quad (5)$$

3.2. Model

We model the galaxy surface density based on a line-of-sight integration of a spherical density profile proposed in B. Diemer (2023, hereafter D23). Previous works traditionally relied on a similar profile from B. Diemer & A. V. Kravtsov (2014, DK14) to fit their density profiles. Both DK14 and D23 can be written as an addition of a profile composed of orbiting galaxies (ρ_{orbit}) and another profile composed of infalling galaxies (ρ_{infall}). These profiles are designed to encapsulate the features of dark matter halos out to large radii where material falling into the gravitational well of the clusters

can be described through an infalling power-law term. D23 improves on the model in DK14, which is traditionally used as a fitting function for splashback analysis in many previous works, by providing more accurate fitting using more free parameters. In this work, we use a modified version of D23 which can be described as

$$\rho(r) = \rho_{\text{orbit}}(r) + \rho_{\text{infall}}(r) \quad (6)$$

where

$$\rho_{\text{orbit}}(r) = \rho_s \exp \left(-\frac{2}{\alpha} \left[\left(\frac{r}{r_s} \right)^\alpha - 1 \right] - \frac{1}{\beta} \left[\left(\frac{r}{r_t} \right)^\beta - \left(\frac{r_s}{r_t} \right)^\beta \right] \right), \quad (7)$$

$$\rho_{\text{infall}}(r) = \delta_1 \left[\left(\frac{\delta_1}{\delta_{\text{max}}} \right)^2 + \left(\frac{r}{r_{\text{pivot}}} \right)^{2s} \right]^{-1/2} \quad (8)$$

and the other terms are defined in Table 2. The modification removes the mean density of the Universe (ρ_m) from the infalling term of D23, as our analysis involves the galaxy density profile instead of the matter density profile measured by weak lensing.

Similar to D. Zurcher & S. More (2019) and R. Murata et al. (2020), we obtain a surface density profile using

$$\Sigma_g(R) = \frac{1}{l_{\text{max}}} \int_0^{l_{\text{max}}} dl \rho \left(\sqrt{R^2 + l^2} \right), \quad (9)$$

where R is the projected radius and l is the projected distance to the cluster. We set $l_{\text{max}} = 40h^{-1}$ Mpc and the pivot radius $r_{\text{pivot}} = 1.5h^{-1}$ Mpc, leaving 8 free parameters ($\alpha, \beta, \rho_s, r_s, r_t, \delta_1, \delta_{\text{max}}$, and s) in our fitting process.

3.3. Model fitting

Following the standard methodology of model fitting for a splashback analysis (S. More et al. 2016; T. Shin et al. 2019, 2021; R. Murata et al. 2020), we fit the model described in §3.2 using a Bayesian approach. The likelihood function is described as

$$\ln L \left[\vec{d} \mid \vec{m}(\theta) \right] = -\frac{1}{2} \left[\vec{d} - \vec{m}(\theta) \right]^T C^{-1} \left[\vec{d} - \vec{m}(\theta) \right], \quad (10)$$

where \vec{d} is the data vector, \vec{m} is the model, $\vec{\theta}$ is the model parameter, and C is the covariance matrix. The data vector is the projected galaxy density profile measured in 40 or 50 radial bins for subsamples below or above $S/N_P = 9$, respectively. We then use a posterior

$$\ln P \left[\vec{\theta} \mid \vec{d} \right] = \ln L \left[\vec{d} \mid \vec{m}(\vec{\theta}) \text{Pr}(\vec{\theta}) \right], \quad (11)$$

Table 2. Prior range for each model parameter in §3.2

Parameters	Prior	Description
$\log \alpha$	$[-3, 1]$	Steepening parameter
$\log \beta$	$[-3, 1]$	Truncation sharpness
$\log \left(\frac{\rho_s}{[h^3 \text{Mpc}^{-3}]} \right)$	$[-2, 5]$	Overdensity at scale radius
$\log \left(\frac{r_s}{[h^{-1} \text{Mpc}]} \right)$	$\log[0.2, 5(8)]$	Scale radius
$\log \left(\frac{r_t}{[h^{-1} \text{Mpc}]} \right)$	$\log[0.2, 5(8)]$	Truncation radius
$\log \left(\frac{\delta_1}{[h^3 \text{Mpc}^{-3}]} \right)$	$[-2, 4]$	Infalling normalization
$\log \left(\frac{\delta_{\max}}{[h^3 \text{Mpc}^{-3}]} \right)$	$[-1, 4]$	Infalling central overdensity
s	$[0.1, 10]$	Infalling slope

NOTE—Radial ranges in parenthesis indicate a different upper limit for subsamples with $S/N_P \geq 9$.

where $\Pr(\vec{\theta})$ is the prior of the model parameters.

We provide the priors used in our fitting process in Table 2. We set generous ranges for our prior to ensure that the best fit can be achieved through our fitting process, considering the difference in the mass and redshift range of our sample compared with other cluster and galaxy surveys that have been previously investigated. We also require that r_t is larger than r_s following D23.

We employ an Affine Invariant Markov Chain Monte Carlo (MCMC) ensemble sampler (J. Goodman & J. Weare 2010) from `emcee` (D. Foreman-Mackey et al. 2013) to sample the posterior of our parameters, as described in Equation 11. We use 50 chains and 6000 steps with a burn-in period of 2500 steps. One set of parameters is retained every 50 steps to construct the final sample, from which we derive the statistical results reported in §4. We ensure convergence by inspecting the time streams of each parameter.

4. RESULTS AND DISCUSSION

We cross-correlate the galaxy sample in §2.2 with MaDCoWS2 clusters, divided into subsamples by redshift and S/N_P . The cross-correlations are transformed into galaxy surface densities and fitted to a density profile using the methodology described in §3. In this section, we investigate the halos of MaDCoWS2 cluster candidates, obtain their splashback radii, and compare our results with those in the literature.

4.1. Density Profiles

We present the best-fit parameters for our cluster subsamples in 3. We explore the DK23 parameter space and its relation to the observed properties of our cluster can-

didates using Spearman’s rank correlation coefficients shown in Figure 6.

In Figure 6, mean signal-to-noise $\overline{S/N_P}$ shows a strong and moderate anti-correlation with the steepening parameter α and the truncation sharpness β , respectively, indicating a shallower and less abrupt transitions for systems with higher S/N_P . Moderate correlations are also found between S/N_P and both ρ_s and r_t , suggesting that higher S/N_P cluster candidates are more centrally dense and truncate at larger radius. The mean redshift \bar{z} shows moderate positive correlations with α , β , r_s , and moderate negative correlations with s , implying steeper truncation, larger central scale radius at higher redshift. For the relation between parameters themselves, α is strongly anti-correlated with ρ_s and moderately anti-correlated with r_t , indicating that less steep profiles are denser and have larger truncation radius. There is also a moderate correlation between ρ_s and δ_1 , suggesting that denser profiles are associated with higher normalization of the infalling component.

Although these correlations provide enticing insight, they are more descriptive of the observed sample. Linking the structural profiles to the underlying astrophysics of clusters requires more caution, as the observed profiles reflect a combination of selection effects, intrinsic cluster properties, and the redshift evolution of the mean density of the universe. A framework for interpreting the relationship between the DK23 parameters and cluster mass and accretion rate is presented in simulated result by B. Diemer (2025), who isolate structural properties of the profiles from other effects by scaling radii with R_{200m} (the radius enclosing a mean density 200 times the mean matter density of the universe). To connect the profile parameters to mass or accretion in a similar manner, MaDCoWS2 will need a precise measurement of R_{200m} . Thus, future work using weak-lensing analyses or simulations to obtain R_{200m} will be essential for making more conclusive statements regarding the relationship between the model parameters and the underlying physical properties of our cluster sample.

Using the fitted parameters we list in Table 3, we show the galaxy surface densities as a function of comoving projected radii in Figure 2, 3, 4, and 5 along with their best fits. We plot the comoving spherical density profiles computed from all MCMC samples.

In Figure 2, 3, 4, and 5, the transitions between inner and outer profiles are apparent in both surface and spherical density profiles. This transition range appears at a larger radius for clusters with larger S/N_P . With these clear transitions, the splashback radius can be detected as the steepest slope as shown later in §4.3.

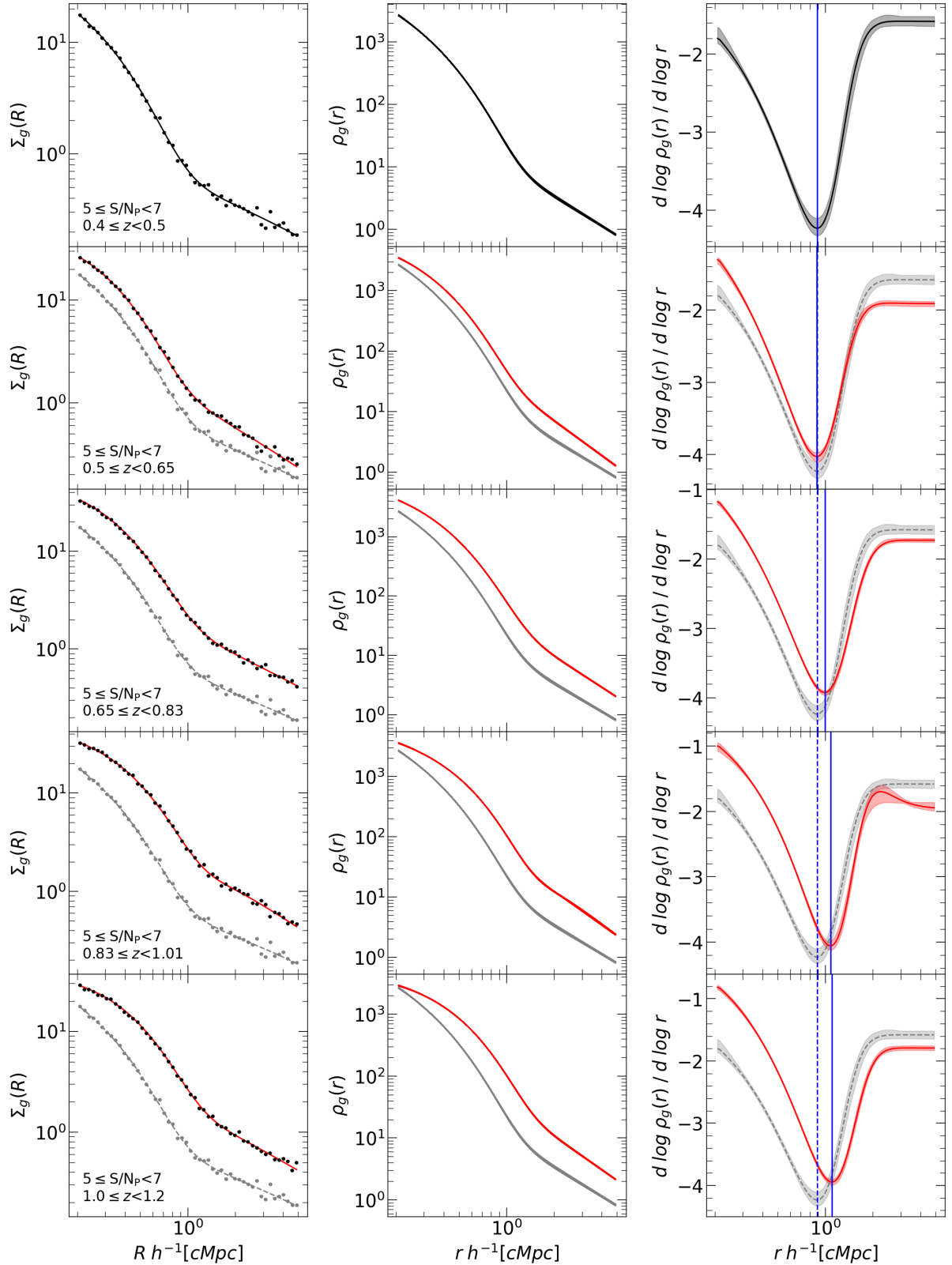


Figure 2. Galaxy surface density versus comoving projected radius (left column), galaxy density versus comoving three-dimensional radius (middle column), and logarithmic derivative of galaxy density versus comoving three-dimensional radius (right column) of MaDCoWS2 clusters with $5 \leq S/N_p < 7$. Each row displays a different redshift subsample as listed in Table 1. The surface density measurements as described in §3.1 are shown as data points in the left column. The solid lines in the left column are the best fit to galaxy surface density from the model fitting scheme in §3.3. The solid lines in the right column show the three-dimensional splashback radii (r_{sp}). For reference, dashed lines show the profiles and splashback radius of the lowest redshift bin in the higher redshift subsamples. We input all fit parameters in our MCMC samples to the model in §3.2 and generate the curves in the middle columns. The curves in the right column correspond to the best-fit parameters, and to the 0th and 100th percentiles of the parameter distribution.

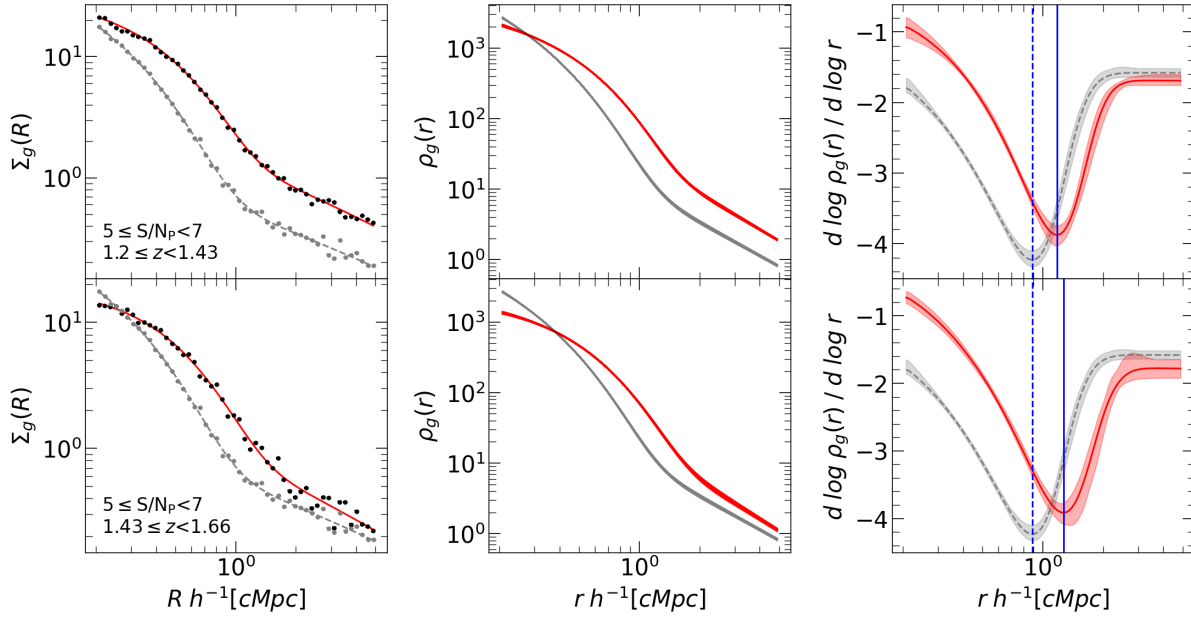


Figure 2. (Continued)

Table 3. Best-fit Parameters for Cluster Subsamples, Measured in Comoving Units

S/N _P	z	$\log \alpha$	$\log \beta$	$\log \rho_s$	$\log r_s$	$\log r_t$	δ_1	δ_{\max}	s
$5 \leq S/N_P < 7$	0.4 – 0.5	$0.05^{+0.02}_{-0.04}$	$-1.39^{+0.62}_{-0.78}$	$2.68^{+0.08}_{-0.02}$	$-0.37^{+0.01}_{-0.03}$	$0.17^{+0.37}_{-0.33}$	$0.73^{+0.01}_{-0.01}$	$2.43^{+1.06}_{-0.91}$	$1.58^{+0.02}_{-0.02}$
	0.5 – 0.65	$0.01^{+0.03}_{-0.03}$	$-0.02^{+0.17}_{-0.14}$	$3.03^{+0.08}_{-0.10}$	$-0.41^{+0.04}_{-0.04}$	$-0.08^{+0.25}_{-0.13}$	$1.09^{+0.01}_{-0.01}$	$1.78^{+0.10}_{-0.08}$	$1.91^{+0.01}_{-0.01}$
	0.65 – 0.83	$0.02^{+0.02}_{-0.02}$	$-0.02^{+0.07}_{-0.08}$	$2.97^{+0.08}_{-0.10}$	$-0.34^{+0.04}_{-0.03}$	$-0.06^{+0.14}_{-0.12}$	$1.20^{+0.01}_{-0.01}$	$2.50^{+0.12}_{-0.64}$	$1.73^{+0.01}_{-0.01}$
	0.83 – 1.0	$0.12^{+0.02}_{-0.02}$	$-0.35^{+0.08}_{-0.10}$	$2.75^{+0.07}_{-0.05}$	$-0.22^{+0.02}_{-0.03}$	$-0.04^{+0.26}_{-0.11}$	$1.39^{+0.01}_{-0.01}$	$1.35^{+0.04}_{-0.03}$	$1.97^{+0.02}_{-0.02}$
	1.0 – 1.2	$0.06^{+0.01}_{-0.01}$	$0.05^{+0.05}_{-0.05}$	$2.79^{+0.08}_{-0.09}$	$-0.27^{+0.03}_{-0.03}$	$0^{+0.15}_{-0.11}$	$1.25^{+0.01}_{-0.01}$	$2.41^{+0.07}_{-0.65}$	$1.79^{+0.01}_{-0.01}$
	1.2 – 1.43	$0.15^{+0.04}_{-0.20}$	$-0.51^{+0.74}_{-0.26}$	$2.48^{+0.10}_{-0.05}$	$-0.19^{+0.02}_{-0.04}$	$0.07^{+0.40}_{-0.20}$	$1.15^{+0.01}_{-0.01}$	$1.97^{+0.13}_{-0.13}$	$1.69^{+0.02}_{-0.02}$
	1.43 – 1.65	$0.05^{+0.02}_{-0.02}$	$0.22^{+0.51}_{-0.25}$	$2.57^{+0.04}_{-0.09}$	$-0.28^{+0.05}_{-0.01}$	$0.43^{+0.17}_{-0.20}$	$0.97^{+0.02}_{-0.02}$	$2.02^{+0.19}_{-0.73}$	$1.78^{+0.04}_{-0.04}$
	7 ≤ S/N _P < 9	$-0.13^{+0.07}_{-0.05}$	$-0.23^{+0.23}_{-0.35}$	$2.89^{+0.24}_{-0.15}$	$-0.40^{+0.05}_{-0.10}$	$0.08^{+0.39}_{-0.28}$	$0.99^{+0.01}_{-0.01}$	$2.65^{+1.00}_{-0.65}$	$1.79^{+0.03}_{-0.02}$
$7 \leq S/N_P < 9$	0.5 – 0.65	$-0.07^{+0.02}_{-0.02}$	$-0.08^{+0.08}_{-0.08}$	$3.20^{+0.11}_{-0.22}$	$-0.42^{+0.09}_{-0.05}$	$0.15^{+0.38}_{-0.35}$	$1.38^{+0.01}_{-0.01}$	$1.80^{+0.05}_{-0.05}$	$2.29^{+0.02}_{-0.02}$
	0.65 – 0.83	$-0.12^{+0.02}_{-0.02}$	$-0.13^{+0.04}_{-0.05}$	$2.96^{+0.11}_{-0.12}$	$-0.26^{+0.04}_{-0.04}$	$-0.03^{+0.16}_{-0.12}$	$1.31^{+0.01}_{-0.01}$	$2.39^{+0.13}_{-0.80}$	$1.62^{+0.02}_{-0.02}$
	0.83 – 1.0	$-0.08^{+0.01}_{-0.01}$	$-0.08^{+0.05}_{-0.04}$	$3.05^{+0.09}_{-0.16}$	$-0.28^{+0.06}_{-0.04}$	$0.23^{+0.29}_{-0.25}$	$1.37^{+0.01}_{-0.01}$	$1.59^{+0.05}_{-0.05}$	$1.70^{+0.02}_{-0.02}$
	1.0 – 1.2	$-0.05^{+0.02}_{-0.02}$	$-0.05^{+0.08}_{-0.09}$	$2.97^{+0.09}_{-0.17}$	$-0.26^{+0.07}_{-0.04}$	$0.29^{+0.28}_{-0.30}$	$1.12^{+0.03}_{-0.03}$	$2.38^{+1.03}_{-0.47}$	$1.29^{+0.04}_{-0.04}$
	1.2 – 1.65	$-0.01^{+0.06}_{-0.04}$	$-0.09^{+0.52}_{-0.32}$	$2.86^{+0.11}_{-0.22}$	$-0.30^{+0.09}_{-0.05}$	$0.26^{+0.29}_{-0.30}$	$1.19^{+0.04}_{-0.05}$	$2.41^{+0.84}_{-0.66}$	$1.60^{+0.07}_{-0.07}$
	S/N _P ≥ 9	$-0.06^{+0.02}_{-0.04}$	$-2.03^{+0.89}_{-0.67}$	$2.62^{+0.05}_{-0.04}$	$-0.25^{+0.02}_{-0.01}$	$0.24^{+0.43}_{-0.33}$	$1.17^{+0.02}_{-0.02}$	$2.20^{+0.16}_{-0.79}$	$1.95^{+0.03}_{-0.04}$
	0.5 – 0.65	$-0.18^{+0.02}_{-0.02}$	$-0.17^{+0.10}_{-0.10}$	$3.29^{+0.11}_{-0.17}$	$-0.40^{+0.07}_{-0.05}$	$0.46^{+0.31}_{-0.37}$	$1.43^{+0.02}_{-0.02}$	$1.60^{+0.05}_{-0.05}$	$2.09^{+0.05}_{-0.04}$
	0.65 – 1.20	$-0.24^{+0.05}_{-0.03}$	$-0.26^{+0.16}_{-0.19}$	$2.99^{+0.21}_{-0.26}$	$-0.21^{+0.10}_{-0.09}$	$0.39^{+0.32}_{-0.30}$	$1.15^{+0.05}_{-0.06}$	$2.44^{+1.00}_{-0.95}$	$1.38^{+0.07}_{-0.07}$

NOTE—We report all parameter estimates as the median with the 68% confidence intervals defined by the 16th and 84th percentiles. Parameter units are the same as in Table 2.

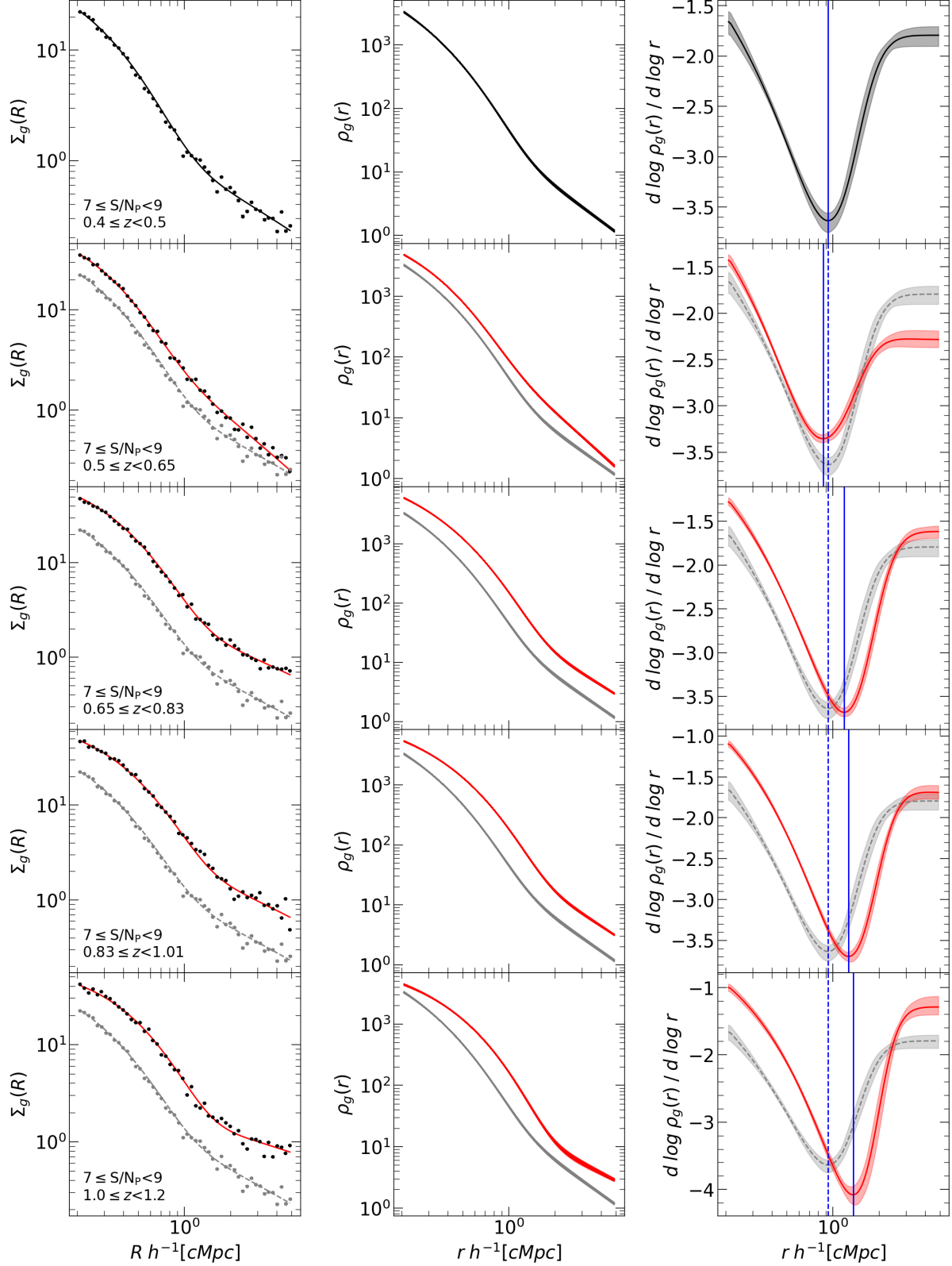


Figure 3. Galaxy surface density (left column), galaxy density (middle column), and logarithmic derivatives of galaxy density (right column) similar to Figure 2, but for subsamples with $7 \leq S/N_p < 9$.

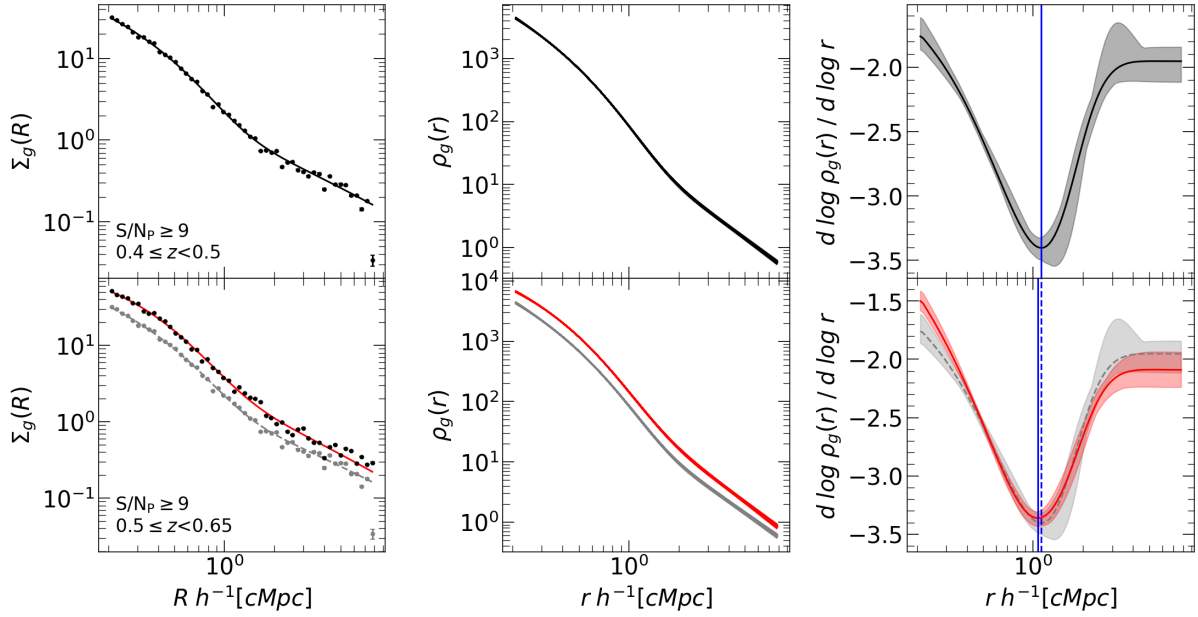


Figure 4. Galaxy surface density (left column), galaxy density (middle column), and logarithmic derivatives of galaxy density (right column) similar to Figure 2, but for subsamples with $S/N_P \geq 9$.

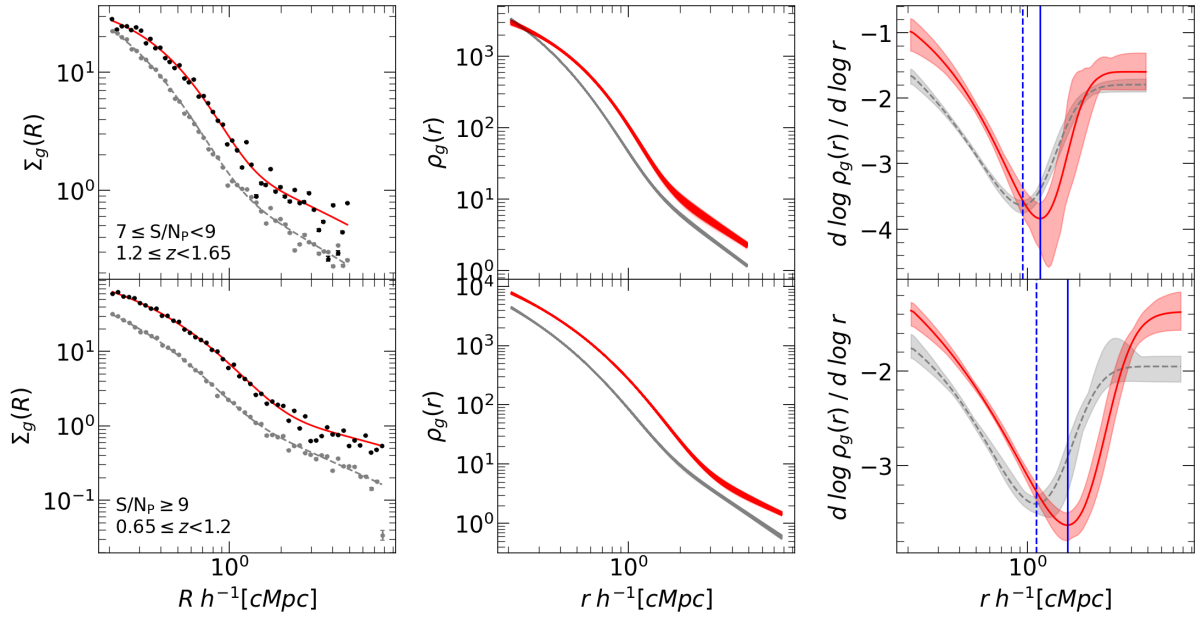


Figure 5. Galaxy surface density (left column), galaxy density (middle column), and logarithmic derivatives of galaxy density (right column) similar to Figure 2, but for $7 \leq S/N_P < 9$ and $S/N_P \geq 9$ with larger redshift binning as described in Table 1.

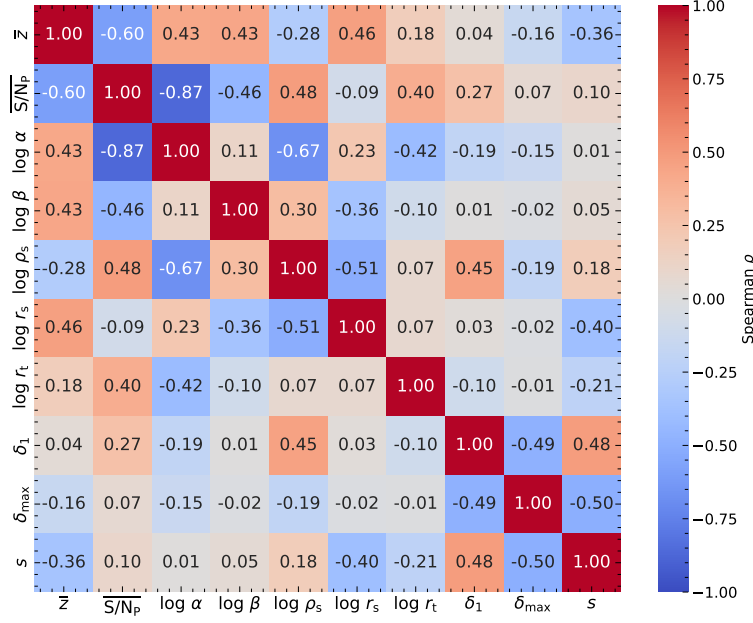


Figure 6. Heatmap of Spearman’s rank correlation coefficient ρ from best-fit parameters in Table 3.

We offer a few interpretations of the density profiles displayed in Figure 2, 3, 4, and 5. First, the structure of the density profiles reflects the fact that cluster candidates detected by MaDCoWS2 are significant overdensities of galaxies compared to the global field. All profiles contain a core with high amplitude that gradually decreases as it extends to a larger radius.

Second, because the density profiles are well-fit by D23, with a clearly visible break in the profile at the splashback radius, we infer that the MaDCoWS2 sample must have a sufficiently high purity over the redshift range so as to not appreciably wash out the signal. This effect is visually evident in the profiles as well as in the splashback radius determination.

Third, the extent of the density profiles agrees with the results in §4.3 and in previous works that clusters with larger S/N_p are generally more extended compared to those with lower S/N_p . The S/N_p scales with the galaxy overdensity at the location of the detection, and is correlated with mass in a similar way to richness at a given redshift. At fixed mass, this S/N will depend weakly on redshift due to any variation in the stellar mass threshold of the galaxy sample. This expectation is supported by the observed positive correlation of S/N_p with M_{500c} from ACT, SPT, Planck, and eRASS in [K. Thongkham et al. \(2024a,b\)](#). Further details on the relation between splashback radius and S/N_p are discussed in §4.3.

Fourth, the Poisson noise associated with a given bin depends on both the number of clusters and the richness of these clusters (i.e., the number of galaxies per clus-

ter). We can therefore improve our splashback radius analysis. The cross-correlations in this work contain small statistical uncertainties, evident in the variation in the data points. However, the typical uncertainty (5%) is small enough that it does not impact the model fitting process. These minor fluctuations result in residuals within the expected noise level, allowing the data to be reliably fit by a two-halo theoretical density profile, such as D23.

4.2. Effect of Uncertainty in Cluster Position and Redshift on Splashback Radius

Table 4. Standard deviations of splashback radius r_{sp} measurements for cluster samples with scatter in position and redshift.

z	$5 \leq S/N_p < 7$	$7 \leq S/N_p < 9$	$S/N_p \geq 9$
0.4-0.5	0.020	0.044	0.167
0.65-0.83	0.025	0.066	...
1.0-1.2	0.027	0.111	...
1.43-1.65	0.045

NOTE—Table is organized by redshift (first column) and S/N_p bins (remaining columns). Each entry shows the standard deviation of the three-dimensional splashback radius r_{sp} measurements from realizations with scatter in both position and redshift.

Given the large sample sizes for the cluster and galaxy catalogs, the statistical uncertainty on the splashback radius is quite small for each bin in S/N and redshift. Nevertheless, the cross-correlations are calculated based on the assumption that the positions and redshifts of cluster detections are exact. In reality, the cluster candidates detected by MaDCoWS2 have uncertainties in both position and redshift. To assess the effect of these uncertainties on the splashback radius determination, we repeat our analysis in §3 for an additional 10 realizations where we include scatter in both position and redshift. The randomization process is based on the uncertainty estimation in K. Thongkham et al. (2024b). For position uncertainty, we randomly shift cluster positions using a multivariate Gaussian distribution with standard deviations of $44''$ and $34''$ in RA and Dec, based on the standard deviations of the offsets between MaDCoWS2 clusters and SPT clusters presented in K. Thongkham et al. (2024a). This is the maximum potential uncertainty from the offsets assuming all the scatter is from MaDCoWS2. For redshift uncertainty, we apply Gaussian scatter to the cluster redshifts using the standard deviation found for MaDCoWS2 photometric redshifts when compared with external spectroscopic redshifts in K. Thongkham et al. (2024a), $\sigma_z/(1+z) = 0.027$. Due to limitations in computational time (10 hours per realization per subsample), we conduct this analysis only for the subsamples displayed in Table 4. We fit the relation between the uncertainty, their redshift, and S/N_p to obtain uncertainties for the remaining subsamples without reanalysis in this section.

We find that shifting cluster positions and redshifts introduces a small change in splashback radius. We report the standard deviation of this set of realizations in Table 4 as a function of the S/N_p and redshift. Randomizing cluster positions flattens the radial profiles due to the fact that field galaxies contribute more. Changing the redshift of the clusters, on the other hand, keeps the clusters at the same position while the clusters are spread across redshift bins. The overdensities still stack closely on the true location, but uncertainty comes from the difference in their sizes across redshifts. Miscentered clusters could also be at incorrect redshifts. To ensure these systematics are accounted for, we thus include the uncertainties from randomization in both redshift and position in our uncertainty calculations throughout the rest of this paper. We note that these uncertainties are likely underestimated, as the model does not fully capture cluster triaxiality, filamentary environments, or correlated large-scale structure.

Table 5. Splashback radii r_{sp} measured in this work

z	$5 \leq S/N_p < 7$	$7 \leq S/N_p < 9$	$S/N_p \geq 9$
	$[h^{-1} \text{ cMpc}]$	$[h^{-1} \text{ cMpc}]$	$[h^{-1} \text{ cMpc}]$
0.4-0.5	$0.89^{+0.02(0.01)}_{-0.02(0.01)}$	$0.93^{+0.05(0.01)}_{-0.05(0.01)}$	$1.12^{+0.17(0.02)}_{-0.17(0.02)}$
0.5-0.65	$0.88^{+0.03(0.01)}_{-0.03(0.01)}$	$0.86^{+0.06(0.01)}_{-0.06(0.01)}$	$1.07^{+0.14(0.03)}_{-0.14(0.03)}$
0.65-0.83	$0.99^{+0.03(0.01)}_{-0.03(0.01)}$	$1.17^{+0.07(0.01)}_{-0.07(0.01)}$...
0.83-1.0	$1.08^{+0.03(0.01)}_{-0.03(0.01)}$	$1.27^{+0.09(0.01)}_{-0.09(0.01)}$...
1.0-1.2	$1.10^{+0.03(0.01)}_{-0.03(0.01)}$	$1.36^{+0.11(0.02)}_{-0.11(0.02)}$...
1.2-1.43	$1.18^{+0.04(0.01)}_{-0.04(0.01)}$
1.43-1.65	$1.27^{+0.05(0.02)}_{-0.05(0.02)}$
1.2-1.65	...	$1.18^{+0.12(0.04)}_{-0.12(0.04)}$...
0.65-1.2	$1.71^{+0.15(0.04)}_{-0.14(0.04)}$

NOTE—The three-dimensional splashback radii measurements are organized by redshift (first column) and S/N_p (three other columns). We report the combined uncertainties from jackknife resampling and those from §4.2 before parentheses. We use quadratic summation to combine the uncertainties. The uncertainties from only jackknife resampling are reported in parentheses.

4.3. Splashback Radius

We follow the description of the splashback radius introduced in S. More et al. (2015) which defines the splashback radius as the location where the cluster density profile is the steepest. We calculate the logarithmic derivatives of the density profiles and show them in Figure 2, 3, 4, and 5. We show our splashback radius estimates as lines of the same colors in these Figures. A strong dip, always extending to $d \log \rho_g / d \log r < -3$, is observed in all subsamples in Figure 2, 3, 4, and 5, indicating a clear signal from the splashback radius (E. Baxter et al. 2017). We show our splashback measurements in Table 5, and plot the splashback radius as determined in the comoving and proper frames as a function of redshift in Figure 7.

We test for a significant trend in splashback radii as a function of redshift by performing a weighted least-squares (WLS) regression using the Python package `statsmodels` (S. Seabold & J. Perktold 2010), focusing on the subsamples with $S/N_p < 9$. The results of this analysis are presented in Table 6. We find that we can reject a flat model with 95% confidence (p-values below 0.05 for almost all analysis configurations). The splashback radius in the comoving frame increases with redshift, which suggests a positive correlation between r_{sp} and redshift in comoving coordinate system. Increases in r_{sp} for higher S/N_p are also observed in almost all red-

Table 6. Linear regression results of three-dimensional splashback radius r_{sp} as a function of redshift z for cluster subsamples with $S/N_P < 9$, shown in both proper and comoving units.

	$5 \leq S/N_P < 7$		$7 \leq S/N_P < 9$	
	Proper	Comoving	Proper	Comoving
R^2	0.87	0.95	0.004	0.64
p -value	0.002	0.0002	0.02	0.06
A	-0.07 ± 0.01	0.37 ± 0.04	-0.02 ± 0.14	0.51 ± 0.19
B	0.63 ± 0.01	0.70 ± 0.03	0.65 ± 0.10	0.69 ± 0.14

NOTE—Each entry reports the linear regression statistics of r_{sp} vs. redshift z for the specified S/N_P and distance convention. Slope A and intercept B are from weighted least-squares fits using inverse-variance weights.

Table 7. The splashback radius from previous works

Reference	Sample	Measurement	Mean Redshift	Mean M_{200m}	r_{sp} [$h^{-1} \text{ cMpc}$]
				[$10^{14} h^{-1} M_{\odot}$]	
C. Chang et al. (2018)	DES RM	Galaxy Profile	0.41	$1.69^{+0.31}_{-0.31}$	$1.13^{+0.07}_{-0.07}$
	DES RM	Weak Lensing	0.41	$1.69^{+0.31}_{-0.31}$	$1.34^{+0.21}_{-0.21}$
D. Zurcher & S. More (2019)	Planck SZ	Galaxy Profile	0.18	$5.87^{+2.47}_{-2.87}$	$1.78^{+0.25}_{-0.29}$
O. Contigiani et al. (2019)	CCCP X-ray	Weak Lensing	0.28	$11.46^{+10.78}_{-6.85}$	$2.36^{+0.74}_{-0.47}$
T. Shin et al. (2019)	DES RM	Galaxy Profile	0.46	$5.10^{+1.56}_{-1.34}$	$1.06^{+0.11}_{-0.09}$
	SPT SZ	Galaxy Profile	0.49	$5.60^{+7.71}_{-5.99}$	$1.24^{+0.57}_{-0.44}$
	ACT SZ	Galaxy Profile	0.49	$5.10^{+4.61}_{-4.43}$	$1.32^{+0.40}_{-0.38}$
R. Murata et al. (2020)	HSC CAMIRA	Galaxy Profile	0.57	$1.71^{+0.08}_{-0.07}$	$1.50^{+0.19}_{-0.18}$
T. Shin et al. (2021)	ACT SZ	Weak Lensing	0.46	$4.62^{+3.50}_{-4.90}$	$1.19^{+0.30}_{-0.42}$
	ACT SZ	Galaxy Profile	0.46	$4.62^{+1.10}_{-2.40}$	$1.13^{+0.09}_{-0.13}$
D. Rana et al. (2023)	eFEDS X-ray	Galaxy Profile	< 0.75	$14.52^{+0.06}_{-0.06}$	$1.45^{+0.30}_{-0.26}$
W. Xu et al. (2024)	ZOU21z2m1	Weak Lensing	0.5	$0.71^{+0.15}_{-0.15}$	$0.60^{+0.25}_{-0.25}$
	ZOU21z2m2	Weak Lensing	0.51	$1.62^{+0.21}_{-0.21}$	$0.97^{+0.45}_{-0.45}$
	YANG21z2m1	Weak Lensing	0.47	$0.37^{+0.16}_{-0.16}$	$0.51^{+0.26}_{-0.26}$
	YANG21z2m2	Weak Lensing	0.47	$0.60^{+0.19}_{-0.19}$	$0.70^{+0.39}_{-0.39}$

NOTE—Results from previous works were standardized as in W. Xu et al. (2024). We include only a subset of results from W. Xu et al. (2024) that explore the mass and redshift ranges similar to our work. The splashback radius is three-dimensional.

shift bins, especially when comparing $S/N_P \geq 9$ to lower S/N_P subsamples. In physical units (or proper frame), the splashback radius decreases with redshift while still exhibiting a positive correlation with S/N_P . This is supported by the fact that we can also reject a flat model with 95% confidence for our results in the proper frame. The difference in the redshift trends of the comoving and proper sizes arises from the $(1+z)$ factor, which accounts for the change in physical scale due to cosmic expansion.

The top panel of Figure 7 highlights the redshift reach of our analysis compared to previous results in the literature from C. Chang et al. (2018); D. Zurcher & S. More (2019); O. Contigiani et al. (2019); T. Shin et al. (2019); R. Murata et al. (2020); T. Shin et al. (2021); D. Rana et al. (2023); W. Xu et al. (2024), also presented in Table 7. With MaDCoWS2, we extend splashback radius measurements based on galaxy density beyond $z > 1$, achieving competitive statistical uncertainties.

Nonetheless, we emphasize that the results shown in Table 5 and the top panel of Figure 7 are specific to the

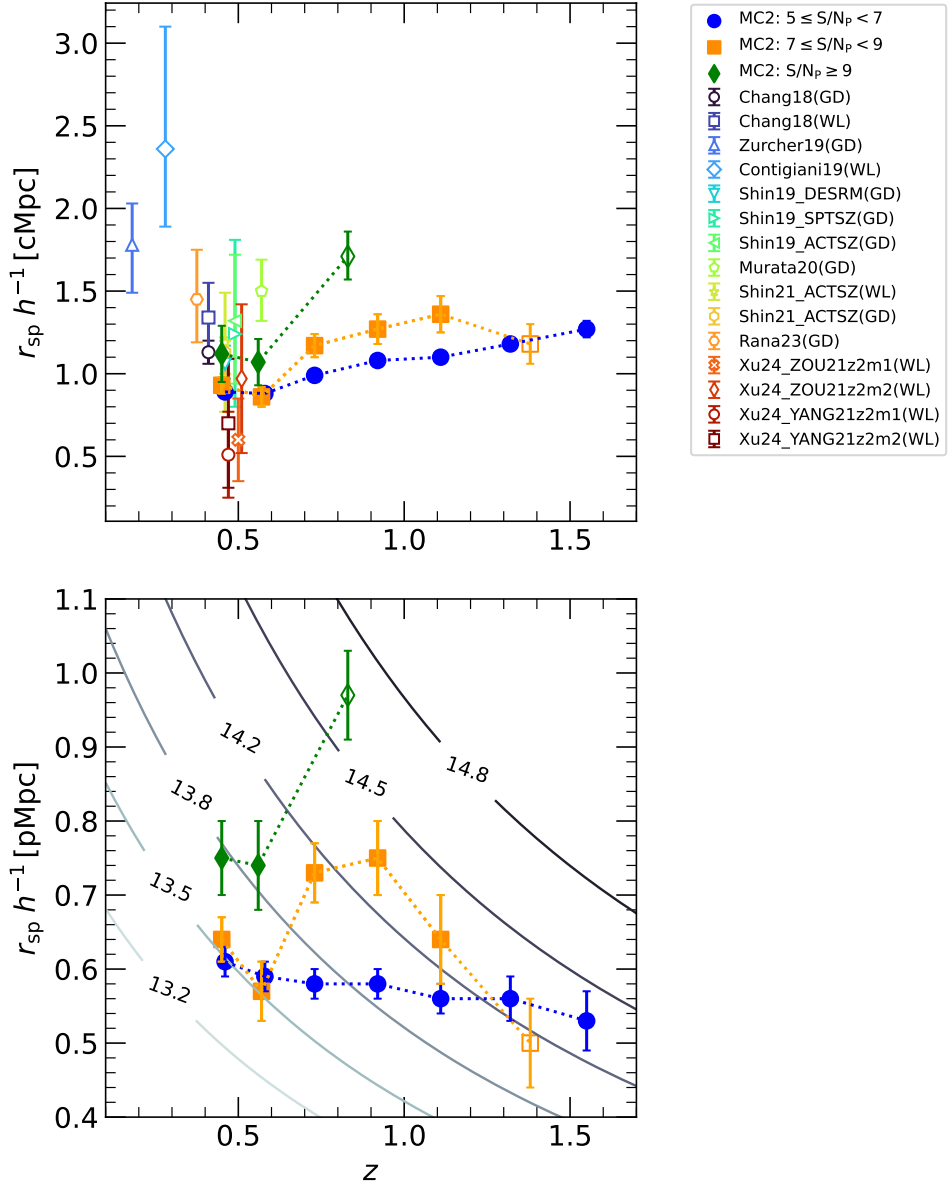


Figure 7. Three-dimensional splashback radius r_{sp} as a function of redshift. Solid blue circles, orange squares, and green diamonds indicate $5 \leq S/N_p < 7$, $7 \leq S/N_p < 9$, and $S/N_p \geq 9$. Open orange square and green diamond indicate binning schemes that cover remaining combined ranges for high- S/N_p subsamples. Errors are estimated from the quadratic summation of uncertainties from jackknife resampling and uncertainties estimated in §4.2. The top panel shows splashback radii determined in comoving frames similar to previous works in the literature in Table 7 (open markers). The bottom panel shows the radius when determined in the proper frame. The contours in the bottom panel show $M_{200\text{m}}$ derived using S. More et al. (2015) splashback model in units of $\log(h^{-1} M_\odot)$.

MaDCoWS2 sample and may be affected by selection effects already mentioned in 4.1, which would benefit from further investigations using weak lensing or simulations.

4.4. Discussion

While the apparent increase of the physical splashback radius (calculated in the proper frame) with decreasing redshift could suggest an evolutionary trend towards more massive clusters that is expected from

the evolution of a halo mass function (J. Tinker et al. 2008; S. Bocquet et al. 2016; G. Despali et al. 2016), the splashback radius depends intricately on peak height (ν), mass, and redshift (S. More et al. 2015; B. Diemer 2025), precluding a straightforward interpretation. To better interpret the relationship between splashback radius, S/N_p , and cluster redshift, we adopt the empirical physical splashback radius–mass relation of S. More et al. (2015), use it to infer cluster masses, and compare

them with estimates from K. Thongkham et al. (2024b) and weak-lensing results from the literature (Table 7).

In S. More et al. (2015), the three-dimensional splashback radius r_{sp} and mass can be calculated by

$$r_{\text{sp}} = 0.81 \left(1 + 0.97e^{\nu/2.44}\right) r_{200m} \quad (12)$$

$$M_{\text{sp}} = 0.82 \left(1 + 0.63e^{\nu/3.52}\right) M_{200m} \quad (13)$$

where ν is the peak height which is defined as $\delta_c/\sigma(M_{200m}, z)$, and $r_{200m}(z)$ is the radius enclosing a mean density 200 times the mean matter density of the universe. We convert the proper splashback radius into M_{200m} using the `splashback.splashbackRadius` function of the COLOSSUS (B. Diemer 2018) package. The function applies the splashback model from S. More et al. (2015) to estimate splashback radius from mass/accretion rate and redshift. The model from S. More et al. (2015) defines the splashback radius as the steepest slope of the density profile, and is calibrated using averaged halo profiles from Λ CDM cosmological simulations. The simulations are run using GADGET2 (V. Springel 2005) described in B. Diemer & A. V. Kravtsov (2014). For each redshift, we construct a grid of M_{200m} and r_{sp} and estimate M_{200m} from a given r_{sp} . We show the mass grid as contour lines in the lower panel of Figure 7. We present the average M_{200m} in a given MaDCoWS2 S/N_P bin as a function of cluster redshift in Table 8. The uncertainties of M_{200m} are estimated from the 1σ upper and lower errors of the three-dimensional splashback radii in physical units.

Table 8. M_{200m} measured from three-dimensional splashback radius r_{sp} in this work using splashback model from S. More et al. (2015)

z	$5 \leq \text{S/N}_P < 7$	$7 \leq \text{S/N}_P < 9$	$\text{S/N}_P \geq 9$
0.4-0.5	$13.49^{+0.05}_{-0.05}$	$13.55^{+0.07}_{-0.07}$	$13.79^{+0.10}_{-0.11}$
0.5-0.65	$13.58^{+0.05}_{-0.05}$	$13.52^{+0.10}_{-0.11}$	$13.91^{+0.12}_{-0.13}$
0.65-0.83	$13.72^{+0.05}_{-0.05}$	$14.08^{+0.08}_{-0.09}$...
0.83-1.0	$13.92^{+0.06}_{-0.06}$	$14.33^{+0.1}_{-0.11}$...
1.0-1.2	$14.05^{+0.06}_{-0.06}$	$14.26^{+0.14}_{-0.16}$...
1.2-1.43	$14.24^{+0.08}_{-0.09}$
1.43-1.65	$14.33^{+0.11}_{-0.12}$
1.2-1.65	...	$14.11^{+0.18}_{-0.20}$...
0.65-1.2	$14.65^{+0.10}_{-0.10}$

NOTE—Similar to Table 1, we organize M_{200m} by redshift (first column) and S/N_P (three other columns). M_{200m} is in the units of $\log(h^{-1}M_{\odot})$.

4.4.1. Comparison with the MaDCoWS2 DR2 Mass-S/N_P Relation

Considering the positive relation between MaDCoWS2 S/N_P and M_{500c} estimated from surveys such as ACT (M. Hilton et al. 2021), SPT (L. E. Bleem et al. 2015; S. Bocquet et al. 2019; L. E. Bleem et al. 2020, 2024), and eRASS (E. Bulbul et al. 2024; M. Kluge et al. 2024) observed in §5.4 of K. Thongkham et al. (2024b), it is expected that subsamples with higher S/N_P in the same redshift range have larger M_{200m} based on the S. More et al. (2015) relation. It is logical that clusters with higher S/N_P, which serves as a proxy for the number density of galaxies in the area, would be more massive.

Additionally, the increase of M_{200m} , derived from S. More et al. (2015) model, with \bar{z} is broadly similar to the fit results reported in K. Thongkham et al. (2024a,b). M_{500c} , derived from ACT, PSZ2 (Planck Collaboration et al. 2016), and eRASS, shows a positive power-law correlation with $1+z$ when fitted as a function of S/N_P. In most relations we investigated in K. Thongkham et al. (2024b), we found an overall increase of cluster M_{500c} , derived from MaDCoWS2 S/N_P and M_{500c} relation, with redshift, even though the slopes and intercepts differ from this work depending on the comparison sample. This apparent increase of M_{200m} and M_{500c} with redshift may partly reflect selection effects connected to photometric catalog limits. Since MaDCoWS2 requires optical detections in addition to CatWISE, the effective luminosity threshold rises with redshift. At the highest redshifts, only the most z -band luminous galaxies are detected, possibly biasing the sample toward more massive clusters that host them (Y. Zhang et al. 2017; S. L. Mulroy et al. 2017).

Although the agreement on the direction of the trends is encouraging, a few caveats are worth noting. First, because of scatter in our mass proxy (S/N_P), the inferred masses are similar for the $5 \leq \text{S/N}_P < 7$ and $7 \leq \text{S/N}_P < 9$ bins. Second, we note that M_{200m} values derived based upon the S. More et al. (2015) relation are systematically lower than those inferred from ACT, SPT, and eRASS calibrations in K. Thongkham et al. (2024a,b). We further explore this offset in the next section.

4.4.2. Comparison with results in literature that include weak-lensing masses

Compared to the comoving splashback radii reported in previous observational studies, as summarized in Table 7, the comoving splashback radii estimated for MaDCoWS2 clusters at $z < 0.75$ are in the middle of the observed mass range. Earlier studies prior to W. Xu

et al. (2024) usually focused on more massive clusters ($M_{200m} \gtrsim 10^{14} h^{-1} M_{\odot}$) to ensure robust statistical analyses, resulting in splashback radius measurements exceeding $1 h^{-1}$ cMpc. On the other hand, the cluster catalogs of W. Xu et al. (2024), constructed from Legacy Surveys and WISE photometric data (H. Zou et al. 2021; X. Yang et al. 2021), are more comparable to MaDCoWS2 in terms of selection and mass range, though a few of their samples include clusters at a lower mass range.

In the context of the comoving splashback radius– M_{200m} relation, our finding that larger comoving splashback radii occur with increasing S/N_p or redshift implies correspondingly larger M_{200m} . This is consistent with the evolution of M_{200m} and M_{500c} with redshift and S/N_p , based on the calculation using relations from S. More et al. (2015) and K. Thongham et al. (2024b), respectively. However, deriving M_{200m} for MaDCoWS2 using the relation from S. More et al. (2015) also results in some discrepancies. At fixed S/N_p , these MaDCoWS2 M_{200m} estimates based on the S. More et al. (2015) relation, especially at $z < 1$, are systematically lower than the expectation from the comoving splashback radius and the weak-lensing M_{200m} in Table 7, as well as our other mass estimates as discussed in the previous section. We fit a power-law model,

$$M_{200m} = ar_{sp}^b \quad (14)$$

to the observed weak-lensing–splashback radius data in Table 7, finding $a = 1.59 \pm 0.36$ and $b = 3.55 \pm 0.50$. Using this relation, the M_{200m} values inferred from our splashback radii are, on average, 2.4, 2.6, and 2.8 times higher than those from the S. More et al. (2015) relation for $5 \leq S/N_p < 7$, $7 \leq S/N_p < 9$, and $S/N_p \geq 9$, respectively. A similar discrepancy was seen in the observed mass ratio–peak height relation of W. Xu et al. (2024), suggesting that the S. More et al. (2015) relation may underestimate M_{200m} in some samples.

Several explanations can be explored for this discrepancy. Our galaxy selection function might select galaxy populations that bias the splashback radii to smaller values (S. Adhikari et al. 2021; S. O’Neil et al. 2022). A related argument is that baryonic effects, such as dynamical friction, may also contribute to the divergence between our results and the S. More et al. (2015) relation in the regime probed by our observational data (E. Xhakaj et al. 2020; T. M. O’Shea et al. 2025). The most plausible explanation likely involves a combination of these effects, together with systematic uncertainties in the observations and assumptions inherent in the simulations.

Our observed evolution of the splashback radius is likely due to a combination of factors rather than purely arising from physical evolution. An improved weak lensing mass calibration and characterization of redshift-dependent selection effects will be important to facilitate the use of the splashback radius as a tool for determining M_{200m} . Such a calibration could be accomplished with deep, wide-field data from the *Euclid* or *Nancy Grace Roman Space Telescope (Roman)* as they become available.

4.5. Future improvement

One potential improvement to the analysis conducted here would be a direct measurement of cluster mass based on a profile that includes all matter. With mass and spherical overdensity radius estimated from weak lensing (i.e., r_{200m}), the splashback radius delivered in this work could be put in a better context. This would improve knowledge of the ratio of splashback radius and weak lensing radius relative to peak height and accretion rate and better validate the relation from cosmological simulations such as S. More et al. (2015); B. Diemer (2025). We could also combine the splashback radius and the shear profile within the radius to calibrate the splashback radius-lensing mass relation.

These improvements could be achieved using shape measurements from the Dark Energy Survey Year 3 (M. Gatti et al. 2021), Kilo Degree Survey (B. Giblin et al. 2021), and the Hyper Supreme Camera wide survey (X. Li et al. 2022), for the redshift and mass range over which weak lensing analyses are possible with these data sets. Further benefits are expected from next-generation facilities such as *Euclid*, the Rubin Observatory, and *Roman*, which will provide higher-precision shape measurements.

5. CONCLUSIONS

We have investigated the galaxy distribution and splashback feature in the MaDCoWS2 cluster sample. Surface density profiles based on cross-correlations of the galaxies from CatWISE2020 and clusters from MaDCoWS2 were measured in different redshift and S/N_p bins. We fit the surface density to a model with orbiting and infalling terms using Bayesian analysis. Using the MCMC samples, we obtained spherical density profiles and determined the splashback radii from their steepest slopes. We summarize our main findings as follows:

- We detect splashback radii out to $z=1.65$, which is the farthest that such a feature has been found. Given the large sample sizes, we are able to derive splashback radii with 2% statistical uncertainties in redshift bins spanning the range $0.4 - 1.65$ and

in multiple S/N_P bins at the low redshift end of this range.

- We confirm that the measured splashback radius increases with S/N_P , consistent with the positive correlation between S/N_P and cluster mass indicated in [K. Thongkham et al. \(2024a,b\)](#).
- We investigate the redshift dependence of the splashback radius, finding that in physical units it decreases by about 13% from $z = 0.4$ to $z = 1.65$ for the lowest S/N_P bin. In comoving units, it increases by 43%.
- Given the redshift dependence of the splashback radius, if we use the scaling relation of [S. More et al. \(2015\)](#) then this implies that the M_{200m} threshold of MaDCoWS2 approximately increases by a factor of 5 from $\bar{z} = 0.46$ to 1.55. A similar positive mass-redshift trend was found in our previous works ([K. Thongkham et al. 2024a,b](#)) although with larger mass. Nevertheless, we note that a more detailed investigation of the selection function from simulations or weak lensing is needed to more robustly explain the evolution of splashback radius and cluster physical properties.
- The redshift dependence of M_{200m} derived here using the [S. More et al. \(2015\)](#) relation has a similar redshift trend to that which was found in [K. Thongkham et al. \(2024a,b\)](#) based on literature masses for SZ and X-ray clusters in MaDCoWS2. The M_{200m} computed using the [S. More et al. \(2015\)](#) relation are however systematically lower than the prediction based on the MaDCoWS2 scaling relations. Additionally, observational calibrations of the $r_{sp} - M_{200m}$ scaling relation using lensing masses indicate that, for a given r_{sp} , the [S. More et al. \(2015\)](#) relation may be underpredicting the masses. A weak-lensing calibration with more robust mass measurements will be crucial to understand this discrepancy.

The analysis in this work shows the statistical power of a large sample of galaxy clusters detected by an algorithm such as PZWav, using the full photometric redshift information, in constraining splashback radii. Nevertheless, future analyses with direct mass measurements are still needed to robustly use splashback radii as a tool for cluster mass estimation. With *Euclid* and Rubin observing a large area of the sky to great depth at high resolution, a better understanding of the halos of galaxy clusters up to high redshift can be achieved in the near future.

ACKNOWLEDGMENTS

This work was supported by the Science and Technology Development Fund of Thailand Science Research and Innovation (TSRI), through the National Astronomical Research Institute of Thailand (Public Organization), Fiscal Year 2025 (ST68), under the project “Enhancing Thailand’s Space Situation through Astronomical Technology” and by the Fundamental Fund of Thailand Science Research and Innovation (TSRI) through the National Astronomical Research Institute of Thailand (Public Organization), Fiscal Year 2026 (FF69). This research was supported by the Korea Astronomy and Space Science Institute under the R&D program (Project No. 2026 – 1 – 831 – 02) supervised by the Korea AeroSpace Administration. This material is based on work supported by the National Science Foundation under Grant No. 2008367. The work of P.E. and D.S. was carried out at the Jet Propulsion Laboratory, California Institute of Technology, under a contract with the National Aeronautics and Space Administration (80NM0018D0004). The authors acknowledge University of Florida Research Computing for providing computational resources and support that have contributed to the research results reported in this publication.

This publication makes use of data products from the *Wide-field Infrared Survey Explorer*, which is a joint project of the University of California, Los Angeles, and the Jet Propulsion Laboratory/California Institute of Technology, funded by the National Aeronautics and Space Administration.

This research has made use of the NASA/IPAC Infrared Science Archive, which is funded by the National Aeronautics and Space Administration and operated by the California Institute of Technology.

This research is based upon the Dark Energy Camera Legacy Survey (DECaLS; PIs: David Schlegel and Arjun Dey). The Legacy Surveys imaging of the DESI footprint is supported by the Director, Office of Science, Office of High Energy Physics of the U.S. Department of Energy under Contract No. DE-AC02-05CH1123, by the National Energy Research Scientific Computing Center, a DOE Office of Science User Facility under the same contract; and by the U.S. National Science Foundation, Division of Astronomical Sciences under Contract No. AST-0950952 to NOAO.

This project used data obtained with the Dark Energy Camera (DECam), which was constructed by the Dark Energy Survey (DES) collaboration. Funding for the DES Projects has been provided by the U.S. Department of Energy, the U.S. National Science Foundation, the Ministry of Science and Education of Spain,

the Science and Technology Facilities Council of the United Kingdom, the Higher Education Funding Council for England, the National Center for Supercomputing Applications at the University of Illinois at Urbana-Champaign, the Kavli Institute of Cosmological Physics at the University of Chicago, Center for Cosmology and Astro-Particle Physics at the Ohio State University, the Mitchell Institute for Fundamental Physics and Astronomy at Texas A&M University, Financiadora de Estudos e Projetos, Fundação Carlos Chagas Filho de Amparo, Financiadora de Estudos e Projetos, Fundação Carlos Chagas Filho de Amparo à Pesquisa do Estado do Rio de Janeiro, Conselho Nacional de Desenvolvimento Científico e Tecnológico and the Ministério da Ciência, Tecnologia e Inovação, the Deutsche Forschungsgemeinschaft and the Collaborating Institutions in the Dark Energy Survey. The Collaborating Institutions are Argonne National Laboratory, the University of California at Santa Cruz, the University of Cambridge, Centro de Investigaciones Enérgéticas, Medioambientales y Tecnológicas–Madrid, the University of Chicago, University College London, the DES-Brazil Consortium, the University of Edinburgh, the Eidgenössische Technische Hochschule (ETH) Zürich, Fermi National Accelerator Laboratory, the University of Illinois at Urbana-Champaign, the Institut de Ciències de l’Espai (IEEC/CSIC), the Institut de Física d’Altes Energies, Lawrence Berkeley National Laboratory, the Ludwig-Maximilians Universität München and the associated Excellence Cluster Universe, the University of Michigan, the National Optical Astronomy Observatory, the University of Nottingham, the Ohio State University, the University of Pennsylvania, the University of Portsmouth, SLAC National Accelerator Laboratory, Stanford University, the University of Sussex, and Texas A&M University.

The Photometric Redshifts for the Legacy Surveys (PRLS) catalog used in this paper was produced thanks to funding from the U.S. Department of Energy Office of Science, Office of High Energy Physics via grant DE-SC0007914.

The Siena Galaxy Atlas was made possible by funding support from the U.S. Department of Energy, Office of Science, Office of High Energy Physics under Award Number DE-SC0020086 and from the National Science Foundation under grant AST-1616414.

Software: PZWav, Astropy ([Astropy Collaboration et al. 2013, 2018, 2022](#)), Matplotlib ([J. D. Hunter 2007](#)), NumPy ([C. R. Harris et al. 2020](#)), pandas ([Pandas Development Team 2023](#); [Wes McKinney 2010](#)), lmfit ([M.](#)

[Newville et al. 2014](#)), SciPy ([P. Virtanen et al. 2020](#)), treecorr ([M. Jarvis et al. 2004; M. Jarvis 2015](#)), emcee ([D. Foreman-Mackey et al. 2013](#)), COLOSSUS ([B. Diemer 2018](#)), statsmodel ([S. Seabold & J. Perktold 2010](#))

APPENDIX

A. PROJECTED SPLASHBACK RADIUS FROM GALAXY SURFACE DENSITY IN PROPER FRAME

In addition to the splashback radii presented in §4.3, we also provide measurements derived from the galaxy surface density, Σ_g , in proper frame. The splashback radius is identified as the location of the steepest slope in the best-fit galaxy surface density profile. These measurements are shown in Table 9. They serve as a basis for comparison with the radii determined from surface brightness profiles presented in [A. Trudeau et al. \(2026\)](#).

Table 9. Splashback radii R_{sp} measured directly from surface densities in proper frame

z	$5 \leq S/N_P < 7$	$7 \leq S/N_P < 9$	$S/N_P \geq 9$
	$[h^{-1} \text{ cMpc}]$	$[h^{-1} \text{ cMpc}]$	$[h^{-1} \text{ cMpc}]$
0.4-0.5	$0.45^{+0.01}_{-0.01}$	$0.48^{+0.02}_{-0.02}$	$0.58^{+0.3}_{-0.03}$
0.5-0.65	$0.46^{+0.01}_{-0.01}$	$0.45^{+0.02}_{-0.02}$	$0.55^{+0.03}_{-0.03}$
0.65-0.83	$0.44^{+0.01}_{-0.01}$	$0.51^{+0.02}_{-0.02}$...
0.83-1.0	$0.45^{+0.01}_{-0.01}$	$0.49^{+0.02}_{-0.02}$...
1.0-1.2	$0.42^{+0.01}_{-0.01}$	$0.46^{+0.03}_{-0.03}$...
1.2-1.43	$0.39^{+0.01}_{-0.01}$
1.43-1.65	$0.40^{+0.02}_{-0.02}$
1.2-1.65	...	$0.39^{+0.02}_{-0.02}$...
0.65-1.2	$0.67^{+0.03}_{-0.03}$

NOTE—Similar to Table 5. The splashback radii measurements are organized by redshift (first column) and S/N_P (three other columns). We report the combined uncertainties from jackknife resampling and those from §4.2.

REFERENCES

Adhikari, S., Dalal, N., & Chamberlain, R. T. 2014, *JCAP*, 2014, 019, doi: [10.1088/1475-7516/2014/11/019](https://doi.org/10.1088/1475-7516/2014/11/019)

Adhikari, S., Shin, T.-h., Jain, B., et al. 2021, *ApJ*, 923, 37, doi: [10.3847/1538-4357/ac0bbc](https://doi.org/10.3847/1538-4357/ac0bbc)

Alberts, S., & Noble, A. 2022, *Univ*, 8, 554, doi: [10.3390/universe811054](https://doi.org/10.3390/universe811054)

Allen, S. W., Evrard, A. E., & Mantz, A. B. 2011, *ARA&A*, 49, 409, doi: [10.1146/annurev-astro-081710-102514](https://doi.org/10.1146/annurev-astro-081710-102514)

Astropy Collaboration, Robitaille, T. P., Tollerud, E. J., et al. 2013, *A&A*, 558, A33, doi: [10.1051/0004-6361/201322068](https://doi.org/10.1051/0004-6361/201322068)

Astropy Collaboration, Price-Whelan, A. M., SipHocz, B. M., et al. 2018, *AJ*, 156, 123, doi: [10.3847/1538-3881/aabc4f](https://doi.org/10.3847/1538-3881/aabc4f)

Astropy Collaboration, Price-Whelan, A. M., Lim, P. L., et al. 2022, *ApJ*, 935, 167, doi: [10.3847/1538-4357/ac7c74](https://doi.org/10.3847/1538-4357/ac7c74)

Baxter, E., Chang, C., Jain, B., et al. 2017, *ApJ*, 841, 18, doi: [10.3847/1538-4357/aa6ff0](https://doi.org/10.3847/1538-4357/aa6ff0)

Bianconi, M., Buscicchio, R., Smith, G. P., et al. 2021, *ApJ*, 911, 136, doi: [10.3847/1538-4357/abebd7](https://doi.org/10.3847/1538-4357/abebd7)

Bleem, L. E., Stalder, B., de Haan, T., et al. 2015, *ApJS*, 216, 27, doi: [10.1088/0067-0049/216/2/27](https://doi.org/10.1088/0067-0049/216/2/27)

Bleem, L. E., Bocquet, S., Stalder, B., et al. 2020, *ApJS*, 247, 25, doi: [10.3847/1538-4365/ab6993](https://doi.org/10.3847/1538-4365/ab6993)

Bleem, L. E., Klein, M., Abbot, T. M. C., et al. 2024, *OJAp*, 7, 13, doi: [10.21105/astro.2311.07512](https://doi.org/10.21105/astro.2311.07512)

Bocquet, S., Saro, A., Dolag, K., & Mohr, J. J. 2016, *MNRAS*, 456, 2361, doi: [10.1093/mnras/stv2657](https://doi.org/10.1093/mnras/stv2657)

Bocquet, S., Dietrich, J. P., Schrabback, T., et al. 2019, *ApJ*, 878, 55, doi: [10.3847/1538-4357/ab1f10](https://doi.org/10.3847/1538-4357/ab1f10)

Bulbul, E., Liu, A., Kluge, M., et al. 2024, *A&A*, 685, A106, doi: [10.1051/0004-6361/202348264](https://doi.org/10.1051/0004-6361/202348264)

Chang, C., Baxter, E., Jain, B., et al. 2018, *ApJ*, 864, 83, doi: [10.3847/1538-4357/aad5e7](https://doi.org/10.3847/1538-4357/aad5e7)

Contigiani, O., Bahé, Y. M., & Hoekstra, H. 2021, *MNRAS*, 505, 2932, doi: [10.1093/mnras/stab1463](https://doi.org/10.1093/mnras/stab1463)

Contigiani, O., Hoekstra, H., & Bahé, Y. M. 2019, *MNRAS*, 485, 408, doi: [10.1093/mnras/stz404](https://doi.org/10.1093/mnras/stz404)

Contigiani, O., Hoekstra, H., Brouwer, M. M., et al. 2023, *MNRAS*, 518, 2640, doi: [10.1093/mnras/stac3027](https://doi.org/10.1093/mnras/stac3027)

Despali, G., Giocoli, C., Angulo, R. E., et al. 2016, *MNRAS*, 456, 2486, doi: [10.1093/mnras/stv2842](https://doi.org/10.1093/mnras/stv2842)

Dey, A., Schlegel, D. J., Lang, D., et al. 2019, *AJ*, 157, 168, doi: [10.3847/1538-3881/ab089d](https://doi.org/10.3847/1538-3881/ab089d)

Diemer, B. 2018, *ApJS*, 239, 35, doi: [10.3847/1538-4365/aaee8c](https://doi.org/10.3847/1538-4365/aaee8c)

Diemer, B. 2023, *MNRAS*, 519, 3292, doi: [10.1093/mnras/stac3778](https://doi.org/10.1093/mnras/stac3778)

Diemer, B. 2025, *MNRAS*, 536, 1718, doi: [10.1093/mnras/stae2717](https://doi.org/10.1093/mnras/stae2717)

Diemer, B., & Kravtsov, A. V. 2014, *ApJ*, 789, 1, doi: [10.1088/0004-637X/789/1/1](https://doi.org/10.1088/0004-637X/789/1/1)

Diemer, B., Mansfield, P., Kravtsov, A. V., & More, S. 2017, *ApJ*, 843, 140, doi: [10.3847/1538-4357/aa79ab](https://doi.org/10.3847/1538-4357/aa79ab)

Eisenhardt, P. R. M., Marocco, F., Fowler, J. W., et al. 2020, *ApJS*, 247, 69, doi: [10.3847/1538-4365/ab7f2a](https://doi.org/10.3847/1538-4365/ab7f2a)

Euclid Collaboration, Adam, R., Vannier, M., et al. 2019, *A&A*, 627, A23, doi: [10.1051/0004-6361/201935088](https://doi.org/10.1051/0004-6361/201935088)

Euclid Collaboration, Bhargava, S., Benoist, C., et al. 2025, arXiv e-prints, arXiv:2503.19196, doi: [10.48550/arXiv.2503.19196](https://doi.org/10.48550/arXiv.2503.19196)

Fabian, A. C. 2012, *ARA&A*, 50, 455, doi: [10.1146/annurev-astro-081811-125521](https://doi.org/10.1146/annurev-astro-081811-125521)

Foreman-Mackey, D., Hogg, D. W., Lang, D., & Goodman, J. 2013, *PASP*, 125, 306, doi: [10.1086/670067](https://doi.org/10.1086/670067)

Gatti, M., Sheldon, E., Amon, A., et al. 2021, *MNRAS*, 504, 4312, doi: [10.1093/mnras/stab918](https://doi.org/10.1093/mnras/stab918)

Giblin, B., Heymans, C., Asgari, M., et al. 2021, *A&A*, 645, A105, doi: [10.1051/0004-6361/202038850](https://doi.org/10.1051/0004-6361/202038850)

Giocoli, C., Palmucci, L., Lesci, G. F., et al. 2024, *A&A*, 687, A79, doi: [10.1051/0004-6361/202449561](https://doi.org/10.1051/0004-6361/202449561)

Gonzalez, A. 2014, in *Building the Euclid Cluster Survey - Scientific Program*, 7

Goodman, J., & Weare, J. 2010, *CAMCoS*, 5, 65, doi: [10.2140/camcos.2010.5.65](https://doi.org/10.2140/camcos.2010.5.65)

Grandis, S., Ghirardini, V., Bocquet, S., et al. 2024, *A&A*, 687, A178, doi: [10.1051/0004-6361/202348615](https://doi.org/10.1051/0004-6361/202348615)

Haggar, R., Amoura, Y., Mpetha, C. T., et al. 2024, *ApJ*, 972, 28, doi: [10.3847/1538-4357/ad5cee](https://doi.org/10.3847/1538-4357/ad5cee)

Harris, C. R., Millman, K. J., van der Walt, S. J., et al. 2020, *Natur*, 585, 357, doi: [10.1038/s41586-020-2649-2](https://doi.org/10.1038/s41586-020-2649-2)

Harrison, C. M., & Ramos Almeida, C. 2024, *Galaxies*, 12, 17, doi: [10.3390/galaxies12020017](https://doi.org/10.3390/galaxies12020017)

Heneka, C., Rapetti, D., Cataneo, M., et al. 2018, *MNRAS*, 473, 3882, doi: [10.1093/mnras/stx2549](https://doi.org/10.1093/mnras/stx2549)

Hilton, M., Sifón, C., Naess, S., et al. 2021, *ApJS*, 253, 3, doi: [10.3847/1538-4365/abd023](https://doi.org/10.3847/1538-4365/abd023)

Hunter, J. D. 2007, *CSE*, 9, 90, doi: [10.1109/MCSE.2007.55](https://doi.org/10.1109/MCSE.2007.55)

Jarvis, M. 2015, *TreeCorr: Two-point correlation functions*, Astrophysics Source Code Library, record ascl:1508.007

Jarvis, M., Bernstein, G., & Jain, B. 2004, *MNRAS*, 352, 338, doi: [10.1111/j.1365-2966.2004.07926.x](https://doi.org/10.1111/j.1365-2966.2004.07926.x)

Kluge, M., Comparat, J., Liu, A., et al. 2024, *A&A*, 688, A210, doi: [10.1051/0004-6361/202349031](https://doi.org/10.1051/0004-6361/202349031)

Landy, S. D., & Szalay, A. S. 1993, *ApJ*, 412, 64, doi: [10.1086/172900](https://doi.org/10.1086/172900)

Li, X., Miyatake, H., Luo, W., et al. 2022, PASJ, 74, 421, doi: [10.1093/pasj/psac006](https://doi.org/10.1093/pasj/psac006)

Mansfield, P., Kravtsov, A. V., & Diemer, B. 2017, ApJ, 841, 34, doi: [10.3847/1538-4357/aa7047](https://doi.org/10.3847/1538-4357/aa7047)

Marocco, F., Eisenhardt, P. R. M., Fowler, J. W., et al. 2021, ApJS, 253, 8, doi: [10.3847/1538-4365/abd805](https://doi.org/10.3847/1538-4365/abd805)

McNamara, B. R., & Nulsen, P. E. J. 2012, New Journal of Physics, 14, 055023, doi: [10.1088/1367-2630/14/5/055023](https://doi.org/10.1088/1367-2630/14/5/055023)

More, S., Diemer, B., & Kravtsov, A. V. 2015, ApJ, 810, 36, doi: [10.1088/0004-637X/810/1/36](https://doi.org/10.1088/0004-637X/810/1/36)

More, S., Miyatake, H., Takada, M., et al. 2016, ApJ, 825, 39, doi: [10.3847/0004-637X/825/1/39](https://doi.org/10.3847/0004-637X/825/1/39)

Mpetha, C. T., Taylor, J. E., Amoura, Y., & Haggard, R. 2024, MNRAS, 532, 2521, doi: [10.1093/mnras/stae1637](https://doi.org/10.1093/mnras/stae1637)

Mpetha, C. T., Taylor, J. E., Amoura, Y., et al. 2025, arXiv e-prints, arXiv:2501.09147, doi: [10.48550/arXiv.2501.09147](https://doi.org/10.48550/arXiv.2501.09147)

Mulroy, S. L., McGee, S. L., Gillman, S., et al. 2017, MNRAS, 472, 3246, doi: [10.1093/mnras/stx2108](https://doi.org/10.1093/mnras/stx2108)

Murata, R., Sunayama, T., Oguri, M., et al. 2020, PASJ, 72, 64, doi: [10.1093/pasj/psaa041](https://doi.org/10.1093/pasj/psaa041)

Newville, M., Stensitzki, T., Allen, D. B., & Ingargiola, A. 2014, LMFIT: Non-Linear Least-Square Minimization and Curve-Fitting for Python, v0.8.0 Zenodo, doi: [10.5281/zenodo.11813](https://doi.org/10.5281/zenodo.11813)

Nishizawa, A. J., Oguri, M., Oogi, T., et al. 2018, PASJ, 70, S24, doi: [10.1093/pasj/psx106](https://doi.org/10.1093/pasj/psx106)

Norberg, P., Baugh, C. M., Gaztañaga, E., & Croton, D. J. 2009, MNRAS, 396, 19, doi: [10.1111/j.1365-2966.2009.14389.x](https://doi.org/10.1111/j.1365-2966.2009.14389.x)

O’Neil, S., Barnes, D. J., Vogelsberger, M., & Diemer, B. 2021, MNRAS, 504, 4649, doi: [10.1093/mnras/stab1221](https://doi.org/10.1093/mnras/stab1221)

O’Neil, S., Borrow, J., Vogelsberger, M., & Diemer, B. 2022, MNRAS, 513, 835, doi: [10.1093/mnras/stac850](https://doi.org/10.1093/mnras/stac850)

O’Shea, T. M., Borrow, J., O’Neil, S., & Vogelsberger, M. 2025, The Open Journal of Astrophysics, 8, E165, doi: [10.33232/001c.147125](https://doi.org/10.33232/001c.147125)

Pacaud, F., Pierre, M., Melin, J. B., et al. 2018, A&A, 620, A10, doi: [10.1051/0004-6361/201834022](https://doi.org/10.1051/0004-6361/201834022)

Pandas Development Team. 2023, pandas-dev/pandas: Pandas, v2.0.3 Zenodo, doi: [10.5281/zenodo.8092754](https://doi.org/10.5281/zenodo.8092754)

Planck Collaboration, Ade, P. A. R., Aghanim, N., et al. 2016, A&A, 594, A27, doi: [10.1051/0004-6361/201525823](https://doi.org/10.1051/0004-6361/201525823)

Planck Collaboration, Aghanim, N., Akrami, Y., et al. 2020, A&A, 641, A6, doi: [10.1051/0004-6361/201833910](https://doi.org/10.1051/0004-6361/201833910)

Rana, D., More, S., Miyatake, H., et al. 2023, MNRAS, 522, 4181, doi: [10.1093/mnras/stad1239](https://doi.org/10.1093/mnras/stad1239)

Rykoff, E. S., Rozo, E., Busha, M. T., et al. 2014, ApJ, 785, 104, doi: [10.1088/0004-637X/785/2/104](https://doi.org/10.1088/0004-637X/785/2/104)

Seabold, S., & Perktold, J. 2010, in 9th Python in Science Conference

Seppi, R., Comparat, J., Nandra, K., et al. 2021, A&A, 652, A155, doi: [10.1051/0004-6361/202039123](https://doi.org/10.1051/0004-6361/202039123)

Shi, X. 2016, MNRAS, 459, 3711, doi: [10.1093/mnras/stw925](https://doi.org/10.1093/mnras/stw925)

Shin, T., Adhikari, S., Baxter, E. J., et al. 2019, MNRAS, 487, 2900, doi: [10.1093/mnras/stz1434](https://doi.org/10.1093/mnras/stz1434)

Shin, T., Jain, B., Adhikari, S., et al. 2021, MNRAS, 507, 5758, doi: [10.1093/mnras/stab2505](https://doi.org/10.1093/mnras/stab2505)

Shin, T.-h., & Diemer, B. 2023, MNRAS, 521, 5570, doi: [10.1093/mnras/stad860](https://doi.org/10.1093/mnras/stad860)

Springel, V. 2005, MNRAS, 364, 1105, doi: [10.1111/j.1365-2966.2005.09655.x](https://doi.org/10.1111/j.1365-2966.2005.09655.x)

Thongkham, K., Gonzalez, A. H., Brodwin, M., et al. 2024a, ApJ, 967, 123, doi: [10.3847/1538-4357/ad3c44](https://doi.org/10.3847/1538-4357/ad3c44)

Thongkham, K., Gonzalez, A. H., Brodwin, M., et al. 2024b, ApJ, 976, 186, doi: [10.3847/1538-4357/ad888c](https://doi.org/10.3847/1538-4357/ad888c)

Tinker, J., Kravtsov, A. V., Klypin, A., et al. 2008, ApJ, 688, 709, doi: [10.1086/591439](https://doi.org/10.1086/591439)

Trudeau, A., Gonzalez, A. H., Thongkham, K., et al. 2024, arXiv e-prints, arXiv:2406.03633, doi: [10.48550/arXiv.2406.03633](https://doi.org/10.48550/arXiv.2406.03633)

Trudeau, A., Gonzalez, A. H., Thongkham, K., et al. 2026, ApJ, in press

Umetsu, K., & Diemer, B. 2017, ApJ, 836, 231, doi: [10.3847/1538-4357/aa5c90](https://doi.org/10.3847/1538-4357/aa5c90)

Vikhlinin, A., Kravtsov, A. V., Burenin, R. A., et al. 2009, ApJ, 692, 1060, doi: [10.1088/0004-637X/692/2/1060](https://doi.org/10.1088/0004-637X/692/2/1060)

Virtanen, P., Gommers, R., Oliphant, T. E., et al. 2020, NatMe, 17, 261, doi: [10.1038/s41592-019-0686-2](https://doi.org/10.1038/s41592-019-0686-2)

von der Linden, A., Wild, V., Kauffmann, G., White, S. D. M., & Weinmann, S. 2010, MNRAS, 404, 1231, doi: [10.1111/j.1365-2966.2010.16375.x](https://doi.org/10.1111/j.1365-2966.2010.16375.x)

Walker, K., Ludlow, A., Power, C., Knebe, A., & Cui, W. 2025, arXiv e-prints, arXiv:2508.07232, doi: [10.48550/arXiv.2508.07232](https://doi.org/10.48550/arXiv.2508.07232)

Watson, W. A., Iliev, I. T., D’Aloisio, A., et al. 2013, MNRAS, 433, 1230, doi: [10.1093/mnras/stt791](https://doi.org/10.1093/mnras/stt791)

Werner, S. V., Cypriano, E. S., Gonzalez, A. H., et al. 2023, MNRAS, 519, 2630, doi: [10.1093/mnras/stac3273](https://doi.org/10.1093/mnras/stac3273)

Wes McKinney. 2010, in Proceedings of the 9th Python in Science Conference, ed. Stéfan van der Walt & Jarrod Millman, 56 – 61, doi: [10.25080/Majora-92bf1922-00a](https://doi.org/10.25080/Majora-92bf1922-00a)

Xhakaj, E., Diemer, B., Leauthaud, A., et al. 2020, MNRAS, 499, 3534, doi: [10.1093/mnras/staa3046](https://doi.org/10.1093/mnras/staa3046)

Xu, W., Shan, H., Li, R., et al. 2024, ApJ, 971, 157, doi: [10.3847/1538-4357/ad57c7](https://doi.org/10.3847/1538-4357/ad57c7)

Yang, X., Xu, H., He, M., et al. 2021, ApJ, 909, 143, doi: [10.3847/1538-4357/abddb2](https://doi.org/10.3847/1538-4357/abddb2)

Zhang, Y., Miller, C. J., Rooney, P., et al. 2017, arXiv e-prints, arXiv:1710.05908, doi: [10.48550/arXiv.1710.05908](https://doi.org/10.48550/arXiv.1710.05908)

Zou, H., Gao, J., Xu, X., et al. 2021, ApJS, 253, 56, doi: [10.3847/1538-4365/abe5b0](https://doi.org/10.3847/1538-4365/abe5b0)
Zurcher, D., & More, S. 2019, ApJ, 874, 184, doi: [10.3847/1538-4357/ab08e8](https://doi.org/10.3847/1538-4357/ab08e8)